

Comparing Hubbard parameters from linear-response theory and Hartree-Fock-based approach

Wooil Yang,^{1,2} Iurii Timrov,^{3,*} Francesco Aquilante,⁴ and Young-Woo Son^{1,†}

¹*Korea Institute for Advanced Study, Seoul 02455, Korea*

²*Oden Institute for Computational Engineering and Sciences,
The University of Texas at Austin, Austin, Texas 78712, USA*

³*PSI Center for Scientific Computing, Theory and Data,*

Paul Scherrer Institute, 5232 Villigen PSI, Switzerland

⁴*Open MOLCAS Community, Geneva 1219, Switzerland*

Density-functional theory with on-site U and inter-site V Hubbard corrections (DFT+ U + V) is a powerful and accurate method for predicting various properties of transition-metal compounds. However, its accuracy depends critically on the values of these Hubbard parameters. Although they can be determined empirically, first-principles methods provide a more consistent and reliable approach; yet, their results can vary, and a comprehensive comparison between methods is still lacking. Here, we present a systematic comparison of two widely used approaches for computing U and V , namely linear-response theory (LRT) and the Hartree-Fock-based pseudohybrid functional formalism, applied to a representative set of oxides (MnO, NiO, CoO, FeO, BaTiO₃, ZnO, and ZrO₂). We find that for partially occupied transition-metal d states, these two methods yield consistent U values, but they differ for nearly empty or fully filled d shells. For O- $2p$ states, LRT always predicts large U values (~ 10 eV), whereas the pseudohybrid formalism produces system-dependent values depending on the level of localization and hybridization for the electronic states. Even larger differences are found for the inter-site V : the former predicts consistently small values (< 1 eV), while the latter produces larger values (~ 3 eV), reflecting its explicit dependence on relative charge redistribution. Our results show that while parallels between these two methods exist, they rely on distinct assumptions for determining U and V , leading to variations in predictions of material properties.

INTRODUCTION

Density-functional theory (DFT) [1, 2] underpins modern first-principles simulations in physics, chemistry, and materials science. Despite its remarkable success, progress hinges on the development of increasingly accurate exchange-correlation (xc) functionals. Standard approximations, such as the local spin-density approximation (LSDA) and spin-polarized generalized-gradient approximation (σ -GGA), are invaluable for many systems, yet they perform poorly for transition-metal (TM) and rare-earth (RE) compounds, where localized d and f states suffer from large self-interaction errors (SIEs) [3, 4]. To address these limitations, several beyond-standard approaches have been introduced. Among the most prominent are Hubbard-corrected DFT (DFT+ U [5–7] and its extension DFT+ U + V [8]), meta-GGA functionals (e.g., SCAN [9] and its variants [10, 11]), and hybrid functionals (e.g., PBE0 [12] and HSE06 [13, 14]). Combinations such as SCAN+ U have also been explored [15–18]. Each strategy embodies a distinct philosophy: DFT+ U selectively corrects partially filled orbitals (typically d and f) [19, 20]; meta-GGA incorporates the kinetic-energy density and satisfies a broad set of exact constraints (17 in the case of SCAN); hybrid functionals mix a fraction of Fock exchange with (semi-

)local functionals. While these methods improve predictive power, they each come with intrinsic trade-offs and limitations [21]. Among them, Hubbard-corrected DFT has become especially popular for its ability to enhance accuracy at modest computational cost [22], provided reliable Hubbard parameters are available. These can be obtained either semi-empirically (by fitting to experimental data or higher-level calculations such as hybrids or GW [23]) or through systematic calibration. Examples include tuning U to reproduce binary metal formation energies [24, 25] or to match properties such as band gaps, magnetic moments, lattice parameters, and enthalpies [26–28].

While semi-empirical fitting of Hubbard parameters can be effective, it becomes impractical in materials discovery where experimental data are unavailable or when multiple target properties must be simultaneously reproduced, sometimes requiring advanced optimization schemes such as Bayesian approaches [29, 30]. A natural alternative is to compute Hubbard parameters from first principles using methods such as constrained DFT (cDFT) [31–39], Hartree-Fock-based schemes [40–45], or the constrained random-phase approximation (cRPA) [46–49]. However, predicted values can differ substantially among these approaches [22, 49, 50], and systematic comparisons of their theoretical foundations remain scarce, although notable progress is beginning to emerge [51]. Moreover, the dependence of U on factors such as Hubbard projector choice, pseudopotentials, oxidation state, and base xc functional further complicates

* Corresponding author: iurii.timrov@psi.ch

† Corresponding author: hand@kias.re.kr

reproducibility [20, 39, 51–53]. Therefore, further work similar to Ref. 51 is needed to systematically compare and benchmark different first-principles approaches for computing Hubbard parameters.

Here, we present a comparative study of two such first-principles approaches. The first is based on cDFT formulated within linear-response theory (LRT) [54], which determines on-site U and inter-site V by enforcing piecewise linearity of the total energy with respect to the occupation of localized orbitals (Hubbard manifold), thereby reducing SIEs [55] and improving predictive accuracy. Standard LRT requires supercell calculations, but its reformulation within density-functional perturbation theory (DFPT) [56, 57] replaces these with monochromatic reciprocal-space perturbations in a unit cell. This substantially reduces computational overhead and has enabled applications to increasingly complex systems [58–65]. The second approach for computing U is the Hartree-Fock-based Agapito, Curtarolo, and Buongiorno Nardelli (ACBN0) functional [43] and its extension to inter-site V dubbed as eACBN0 [44, 45], which derives Hubbard parameters directly within self-consistent-field (SCF) cycles from an approximate form of the screened Hartree-Fock interaction energy. Using projections of Kohn-Sham (KS) states onto localized orbitals, U and V are updated at each iteration of the SCF cycle with negligible additional cost relative to standard DFT. This method has been shown to capture electronic structures and dynamical properties with good accuracy [66, 67], and it holds promise for accurate evaluations of electron-phonon interactions [68, 69].

The DFT+U+V approach.

In DFT+ $U+V$ [8, 22], a corrective Hubbard energy E_{U+V} is added to the standard DFT energy E_{DFT} :

$$E_{\text{DFT}+U+V} = E_{\text{DFT}} + E_{U+V}. \quad (1)$$

Unlike DFT+ U , which only accounts for on-site interactions scaled by U , DFT+ $U+V$ also includes inter-site interactions between an atom and its neighbors, scaled by V . In the simplified rotationally-invariant formulation [7], the extended Hubbard correction reads [57]:

$$E_{U+V} = \frac{1}{2} \sum_I \sum_{\sigma mm'} U^I (\delta_{mm'} - n_{mm'}^{II\sigma}) n_{m'm}^{II\sigma} - \frac{1}{2} \sum_I \sum_{J(J \neq I)}^* \sum_{\sigma mm'} V^{IJ} n_{mm'}^{IJ\sigma} n_{m'm}^{JI\sigma}, \quad (2)$$

where I and J index atomic sites, m and m' denote magnetic quantum numbers, and U^I and V^{IJ} are the effective on-site and inter-site Hubbard parameters, respectively. The asterisk denotes that, for each atom I , the sum over J includes all neighbors up to a defined cut-off distance. The generalized occupation matrices $n_{mm'}^{IJ\sigma}$

are obtained by projecting KS states $\psi_{v,\mathbf{k}}^\sigma$ onto localized orbitals $\phi_m^I(\mathbf{r})$:

$$n_{mm'}^{IJ\sigma} = \sum_{v,\mathbf{k}} f_{v,\mathbf{k}}^\sigma \langle \psi_{v,\mathbf{k}}^\sigma | \phi_{m'}^J \rangle \langle \phi_m^I | \psi_{v,\mathbf{k}}^\sigma \rangle, \quad (3)$$

where v and σ label bands and spin, \mathbf{k} runs over the first Brillouin zone (BZ), and $f_{v,\mathbf{k}}^\sigma$ are the KS occupations. In Eq. (3), $m \in I$ and $m' \in J$, meaning that m runs over the magnetic quantum numbers associated with a fixed principal quantum number n and orbital angular momentum l of atom I , and analogously m' for atom J . The corresponding generalized KS equation can be written as [8],

$$(\hat{\mathcal{H}}_{\text{KS}}^\sigma + \hat{\mathcal{V}}_{U+V}^\sigma) |\psi_{v,\mathbf{k}}^\sigma\rangle = \varepsilon_{v,\mathbf{k}}^\sigma |\psi_{v,\mathbf{k}}^\sigma\rangle, \quad (4)$$

where $\hat{\mathcal{H}}_{\text{KS}}^\sigma$ is the KS Hamiltonian of the standard DFT, $\varepsilon_{v,\mathbf{k}}^\sigma$ is the v -th band energy at momentum \mathbf{k} and spin σ , and $\hat{\mathcal{V}}_{U+V}^\sigma$ is the Hubbard potential that is derived from the Hubbard energy (2) and which reads [57]:

$$\begin{aligned} \hat{\mathcal{V}}_{U+V}^\sigma = & \sum_I \sum_{mm'} \frac{U^I}{2} (\delta_{mm'} - 2n_{mm'}^{II\sigma}) |\phi_m^I\rangle \langle \phi_{m'}^I| \\ & - \sum_I \sum_{J(J \neq I)}^* \sum_{mm'} V^{IJ} n_{mm'}^{IJ\sigma} |\phi_m^I\rangle \langle \phi_{m'}^J|. \end{aligned} \quad (5)$$

In Eqs. (2) and (5), the on-site U^I and inter-site V^{IJ} terms act in opposition: the on-site term favors electron localization on atomic sites and suppresses hybridization, whereas the inter-site term enhances hybridization with neighboring atoms. Accurate first-principles evaluation of U^I and V^{IJ} is therefore crucial to correctly describe the balance between localization and hybridization.

It is important to note that the computed values of U^I and V^{IJ} depend on the choice of Hubbard projector functions $\phi_m^I(\mathbf{r})$ used to define the occupation matrix in Eq. (3) and the Hubbard potential in Eq. (5) [44, 52, 70]. In the following, we briefly describe how Hubbard parameters are defined and computed within LRT and eACBN0. For both methods, we employ the same projector functions, namely atomic orbitals orthogonalized using the Löwdin method [71, 72], to ensure a fair and consistent comparison of the computed U^I and V^{IJ} values.

Hubbard parameters from LRT.

Within the LRT framework, Hubbard parameters are defined from the piecewise linearity condition of the total energy [Eq. (1)] with respect to the occupation of the Hubbard manifold and computed as [8, 54]:

$$U^I = (\chi_0^{-1} - \chi^{-1})_{II}, \quad (6)$$

and

$$V^{IJ} = (\chi_0^{-1} - \chi^{-1})_{IJ}, \quad (7)$$

where χ_0 and χ are the bare and self-consistent response matrices, describing how the occupation matrices respond to localized electronic perturbations. The self-consistent response matrix is given by

$$\chi_{IJ} = \sum_{m\sigma} \frac{dn_{mm'}^{I\sigma}}{d\alpha^J}, \quad (8)$$

where $n_{mm'}^{I\sigma} \equiv n_{mm'}^{II\sigma}$ denotes the on-site occupation matrix, and α^J is the strength of the perturbation on the J th site. The bare response χ_0 is defined analogously but evaluated before the self-consistent adjustment of the Hartree and xc potentials.

DFPT allows this calculation to be performed without supercells, by reformulating LRT in terms of monochromatic reciprocal-space perturbations in the unit cell. This significantly reduces computational cost [56, 57]. The response of the occupation matrix is then computed as:

$$\frac{dn_{mm'}^{I\sigma}}{d\alpha^J} = \frac{1}{N_{\mathbf{q}}} \sum_{\mathbf{q}}^{N_{\mathbf{q}}} e^{i\mathbf{q} \cdot (\mathbf{R}_l - \mathbf{R}_{l'})} \Delta_{\mathbf{q}}^{s'} n_{mm'}^{s\sigma}, \quad (9)$$

where \mathbf{q} is the wavevector of the monochromatic perturbation, $N_{\mathbf{q}}$ is the total number of perturbations, and $\Delta_{\mathbf{q}}^{s'} n_{mm'}^{s\sigma}$ is the lattice-periodic response of the occupation matrices to a \mathbf{q} -specific perturbation. Here, $I \equiv (l, s)$ and $J \equiv (l', s')$, with s and s' indexing atoms within the unit cell and l and l' indexing unit cells; \mathbf{R}_l and $\mathbf{R}_{l'}$ are the corresponding Bravais lattice vectors. The quantities $\Delta_{\mathbf{q}}^{s'} n_{mm'}^{s\sigma}$ are obtained from the response KS wavefunctions, which are computed by solving \mathbf{q} -specific Sternheimer equations. Further details on the DFPT implementation can be found in Refs. 56, 57. The efficiency of DFPT for calculating U^I and V^{IJ} has been demonstrated in numerous studies, with several recent highlights [73–78].

Hubbard parameters from eACBN0.

In the eACBN0 method, the Hubbard parameters are defined by equating the corrective Hubbard energy [Eq. (2)] with the Hartree-Fock interaction energy [43, 44]. This leads to the following expressions:

$$U^I = \frac{\sum_{\{m\},\sigma\sigma'} \bar{P}_{mm'}^{II,\sigma} \bar{P}_{m''m'''}^{II,\sigma'} (mm'|m''m''')}{\sum_{mm',\sigma} n_{mm'}^{II,\sigma} n_{m'm'}^{II,-\sigma} + \sum_{m \neq m',\sigma} n_{mm'}^{II,\sigma} n_{m'm'}^{II,\sigma}},$$

$$- \frac{\sum_{\{m\},\sigma} \bar{P}_{mm'}^{II,\sigma} \bar{P}_{m''m'''}^{II,\sigma'} (mm''|m''m')}{\sum_{m \neq m',\sigma} n_{mm'}^{II,\sigma} n_{m'm'}^{II,\sigma}}, \quad (10)$$

and

$$V^{IJ} = \frac{1}{2} \frac{\sum_{mm',\sigma\sigma'} [\bar{P}_{mm'}^{II,\sigma} \bar{P}_{m'm'}^{JJ,\sigma'} - \delta_{\sigma\sigma'} \bar{P}_{mm'}^{IJ,\sigma} \bar{P}_{m'm'}^{JI,\sigma'}]}{\sum_{mm',\sigma\sigma'} (n_{mm'}^{II,\sigma} n_{m'm'}^{JJ,\sigma'} - \delta_{\sigma\sigma'} n_{mm'}^{IJ,\sigma} n_{m'm'}^{JI,\sigma'})} \times (mm|m'm'), \quad (11)$$

where $(mm'|m''m''')$ represents the bare Coulomb interaction between electrons with m, m' of atom I and m'', m''' of atom J . The renormalized density matrix $\bar{P}_{mm'}^{IJ,\sigma}$ is defined as

$$\bar{P}_{mm'}^{IJ,\sigma} = \sum_{v,\mathbf{k}} f_{v,\mathbf{k}}^{\sigma} \bar{N}_{v,\mathbf{k}}^{IJ,\sigma} \langle \psi_{v,\mathbf{k}}^{\sigma} | \phi_{m'}^J \rangle \langle \phi_m^I | \psi_{v,\mathbf{k}}^{\sigma} \rangle, \quad (12)$$

where $\bar{N}_{v,\mathbf{k}}^{IJ,\sigma}$ is the renormalized occupation number defined as

$$\bar{N}_{v,\mathbf{k}}^{IJ,\sigma} = \sum_{\{I\}} \sum_m \langle \psi_{v,\mathbf{k}}^{\sigma} | \phi_m^I \rangle \langle \phi_m^I | \psi_{v,\mathbf{k}}^{\sigma} \rangle + \sum_{\{J\}} \sum_{m'} \langle \psi_{v,\mathbf{k}}^{\sigma} | \phi_{m'}^J \rangle \langle \phi_{m'}^J | \psi_{v,\mathbf{k}}^{\sigma} \rangle, \quad (13)$$

where $m \in I$ and $m' \in J$, and the summations $\sum_{\{I\}}$ and $\sum_{\{J\}}$ mean that we sum up contributions coming from all equivalent atoms of the same type. For the case of U^I -only calculations ($I = J$), the second term in Eq. (13) is dropped [44], so $\bar{N}_{v,\mathbf{k}}^{II,\sigma}$ reduces to the Mulliken charge of atom I in state $\psi_{v,\mathbf{k}}^{\sigma}(\mathbf{r})$. Moreover, $\bar{N}_{v,\mathbf{k}}^{IJ,\sigma}$ can be viewed as a position-dependent mixing parameter within the Hartree-Fock approximation, encoding on-site and inter-site screening effects in the localized subspace. It is important to note that for a fixed ground-state density, the U^I values computed in ACBN0 remain unchanged upon inclusion of inter-site V^{IJ} terms in eACBN0. However, in self-consistent implementations of eACBN0, a coupling between U^I and V^{IJ} emerges because the ground state is obtained under the influence of both on-site and inter-site terms in the Hubbard potential (5), with self-consistency enforced for both the electron density and the Hubbard parameters. Further details on the eACBN0 formalism can be found in Refs. 43–45.

RESULTS

In this section, we present results for the computed on-site U and inter-site V Hubbard parameters across three classes of systems: *i*) TM oxides with partially occupied d states (MnO, FeO, CoO, and NiO); *ii*) compounds with nominally empty d states (ZrO₂ and BaTiO₃); and *iii*) a compound with fully occupied d states (ZnO). These categories allow us to assess similarities and differences between LRT and eACBN0 under distinct electronic configurations.

Hubbard parameters can be computed at different levels of self-consistency. The simplest approach is a

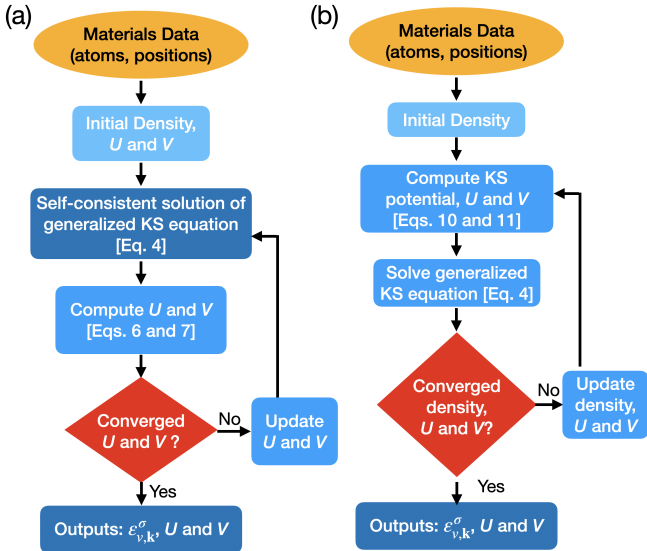


FIG. 1. Protocol for computing Hubbard parameters within the “self-consistent” scheme using (a) LRT (DFPT) [57] and (b) eACBN0 [44]. In the LRT workflow, Hubbard parameters are evaluated self-consistently after the electronic charge density has been fully converged. In contrast, the eACBN0 scheme updates the charge density and the Hubbard parameters simultaneously until convergence is reached. In both workflows, atomic positions are fixed and no structural relaxations are performed.

“one-shot” calculation, where the parameters are evaluated using the converged DFT charge density while keeping the geometry fixed. A more advanced “self-consistent” approach iteratively updates both the charge density and the corresponding U and V values, but still at a fixed geometry. Finally, in the “structurally self-consistent” scheme, structural relaxations (atomic positions and unit-cell parameters) are included in the self-consistent cycle [57, 75]. In the main text, we report results obtained with the “self-consistent” scheme, i.e. calculations in which the electronic degrees of freedom are converged together with the Hubbard parameters while the geometry remains fixed. In this approach, all U and V values are determined consistently with the self-consistent charge density [44, 57], as illustrated in Fig. 1. This allows us to isolate purely electronic effects from structural ones and to assess the influence of extended Hubbard interactions in LRT and eACBN0 with high internal consistency. For completeness, in the Supplemental Information (SI) we also present results obtained using the “structurally self-consistent” scheme, in which the self-consistent cycle includes full structural optimization with updated Hubbard parameters and charge density (see Fig. S1 in the SI). In this case, the crystal structure, the Hubbard parameters, and the charge density are iterated to convergence, yielding mutually consistent electronic and crystal structures. All computational details are provided in the Methods section.

We note that results obtained using the “one-shot”

scheme are not reported in this work. In this scheme, the occupation matrices of Eq. (3) and Kohn-Sham wavefunctions employed to compute the Hubbard parameters (via Eqs. (6) and (7) for LRT and Eqs. (10) and (11) for eACBN0) differ from those that are obtained during the final DFT+ U + V ground-state SCF calculation, which is determined by the Hubbard energy [Eq. (2)] and the Hubbard potential [Eq. (5)]. This difference between the Hubbard parameters evaluation step and the subsequent materials-property calculations makes the “one-shot” scheme not consistent. Moreover, the eACBN0 method is never used in a “one-shot” form in practice. To avoid potential ambiguity for the reader, we therefore do not include “one-shot” results in this work.

Using the computed self-consistent Hubbard parameters, we perform DFT+ U and DFT+ U + V calculations to evaluate various material properties. The band gap serves as our primary benchmark for accuracy. For magnetic oxides we also examine magnetic moments, while for BaTiO₃ we additionally analyze structural properties relevant to ferroelectricity. The results are systematically compared.

Since the band gap is central to this study, it is useful to recall that DFT is not a spectral theory. Local and semilocal xc functionals (LSDA, σ -GGA) notoriously underestimate band gaps in transition-metal oxides (TMOs) due to strong SIEs, particularly on TM ions. DFT+ U can alleviate this issue, but only when the correction is applied to states that define the gap edges (for insulators) or to states near the Fermi level (for spurious DFT metals) [70]. The inter-site V correction can further improve band gaps in covalent systems, but again only when applied to orbitals directly involved in gap formation. Prior work supports these points: Ref. 70 showed that DFT+ U with LRT-derived U improves agreement with experimental band gaps compared to (semi-)local functionals, while DFT+ U + V with LRT-derived parameters yields even better accuracy in TMOs with strong covalency [52, 58, 59, 61]. For p -block semiconductors without TM ions, Ref. 44 demonstrated that DFT+ U + V with eACBN0-derived parameters accurately reproduces experimental band gaps. These insights provide the foundation for our analysis below.

MnO, FeO, CoO, and NiO

TMOs are well-known systems where SIEs are prominently manifested due to localized 3d orbitals. Standard DFT calculations at the LDA or GGA level typically exhibit considerable discrepancies compared to experimental measurements, necessitating the use of the DFT+ U or DFT+ U + V method. Particularly, 3d electrons of TM ions exhibit significant spatial localization, thus requiring Hubbard U corrections, while V might be necessary to describe their hybridization with ligands. Therefore, we select representative 3d TMOs – MnO, FeO, CoO, and NiO – as first targets and apply two Hubbard parameter

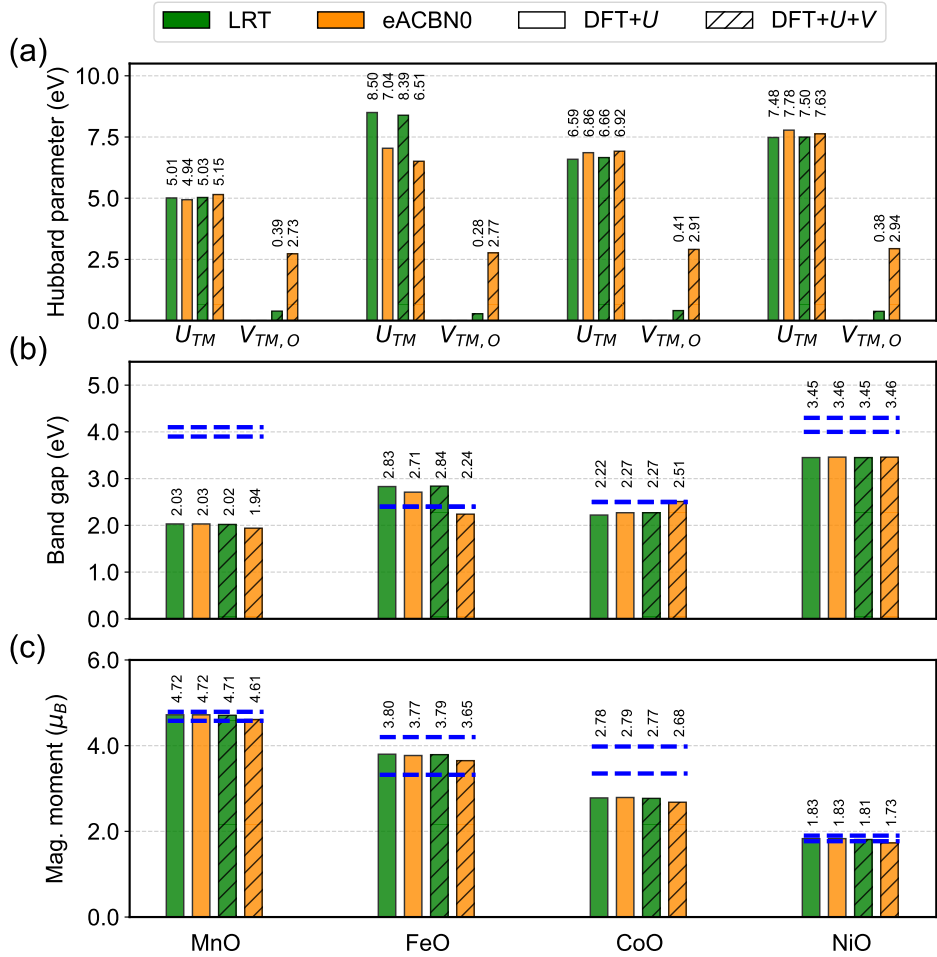


FIG. 2. DFT+U and DFT+U+V self-consistent calculations for TMOs without on-site corrections on O-2p states (U_O), using the workflow described in Fig. 1. (a) On-site Hubbard U_{TM} parameter for 3d orbitals of TM ions and inter-site Hubbard $V_{TM,O}$ parameter between 3d orbitals of TM ions and 2p orbitals of oxygen, (b) band gap, and (c) magnetic moment. LRT and eACBN0 denote the method used to obtain the Hubbard parameters. The experimental band gaps and magnetic moments for MnO [79–82], FeO [83–85], CoO [86–88], and NiO [79, 81, 82, 89] are indicated by the dashed blue lines in panels (b) and (c), respectively.

calculation methods, LRT and eACBN0, to understand the trends in Hubbard parameters and their influence on materials properties such as band gaps and magnetic moments.

To compare the two methods under as equivalent conditions as possible, we perform LRT and eACBN0 calculations using the “self-consistent” scheme described in Fig. 1 and report the Hubbard parameters in Figs. 2 and 3. We focus first on the U values shown as bar plots (unhatched) in Fig. 2 obtained in the framework of the DFT+U method. A clear trend emerges where U_{TM} increases and magnetic moment decreases with the number of 3d electrons. Furthermore, both calculation methods do not alter the U_{TM} values significantly when the inter-site interactions are included (compare the hatched and not hatched patterns in Fig. 2(a)). Focusing on MnO, the dominant Mn-4s character of the lowest conduction band turns out to be insensitive to the Hubbard U parameter

applied to Mn-3d states. The primary role of U_{TM} is to enhance the splitting between occupied and unoccupied Mn-3d states. This is confirmed by the partial density of states (PDOS), which shows that with increasing U_{TM} , occupied d states shift to lower energies, while the unoccupied d states (lying above the conduction band minimum) shift to higher energies [67]. This mechanism is found to be general for other late TMOs like FeO, CoO, and NiO, which also exhibit a prominent TM-4s character at the conduction band minimum at the Γ point. For these materials, we consistently observe that while the energy splitting between occupied and unoccupied d states scales proportionally with U_{TM} , the variation in the fundamental band gap remains minor in comparison.

When the inter-site Hubbard interactions ($V_{TM,O}$) between TM 3d and oxygen 2p states are included, the differences between the two methods remain almost unchanged. In Fig. 2, the results with the $V_{TM,O}$ term are

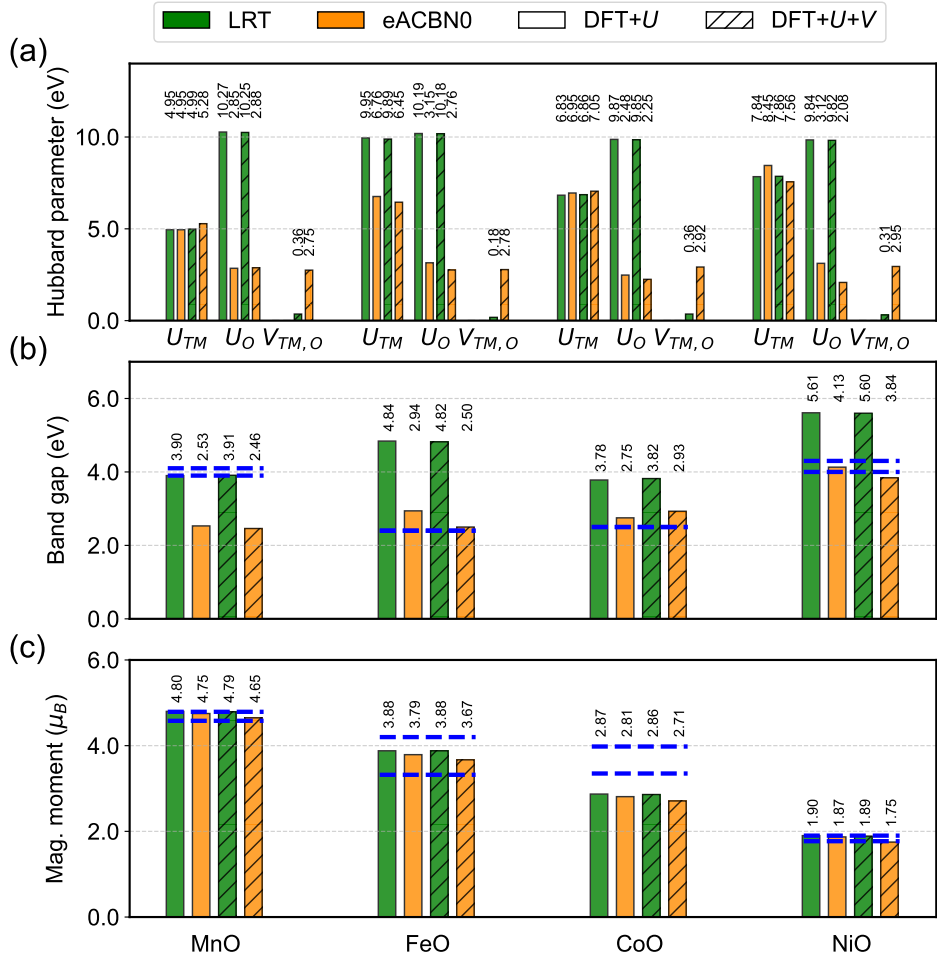


FIG. 3. DFT+U and DFT+U+V self-consistent calculations for TMOs with on-site U_O corrections on O-2p states. The remainder of the caption is analogous to Fig. 2.

illustrated with hatched patterns. LRT yields relatively small $V_{TM,O}$ values (below 1 eV), resulting in negligible differences in band gaps and magnetic moments whether $V_{TM,O}$ term is included or not in the total energy calculation. In contrast, eACBN0 consistently produces larger $V_{TM,O}$ values (close to 3 eV) across all TMOs, resulting in more noticeable changes in band gaps compared to LRT, while the magnetic moments change by a small margin. This effect arises because the $V_{TM,O}$ term facilitates electron delocalization into the overlapping regions between atomic pairs. This counteracts the strong localization favored by the U_{TM} term and thus reduces the local magnetic moment, as previously shown through charge density difference analysis in our earlier studies [67].

Figure 3 extends our analysis by including a Hubbard correction on the oxygen 2p states (U_O), computed with both LRT and eACBN0. Within LRT, the resulting U_O values are large (~ 10 eV), consistently with previous studies [70]. This is a consequence of the high electronegativity of oxygen: its 2p shell is nearly fully occupied, which leads to a weak electronic response and therefore

a large U in the LRT framework [73, 90]. Despite these large U_O values, the inter-site interaction $V_{TM,O}$ remains small (below 1 eV), indicating that TM–O hybridization has only a minor effect on the electronic structure of these TMOs even when U_O is considered. In LRT, U_{TM} and U_O appear as diagonal elements, and $V_{TM,O}$ as off-diagonal elements of the matrix obtained by inverting the interacting and non-interacting response matrices, χ and χ_0 [Eqs. (6) and (7)]. Including oxygen among the perturbed subspaces alters the full response matrices, because screening channels involving O are now explicitly taken into account. Once both TM and O sites are perturbed, the structure of the response matrices in DFT+U and DFT+U+V becomes effectively similar: both schemes capture the same screening pathways involving TM and O states. Consequently, the value of U_{TM} can change when U_O is included in the LRT calculation. Comparing Figs. 2 and 3, we observe a slight increase of U_{TM} for CoO and NiO (by 3–5%), a substantial increase for FeO (18%), and almost no change for MnO. Conversely, eACBN0 yields smaller U_O values than LRT

ones, in the range of 2 – 3 eV. Similar to the case with the $V_{TM,O}$ correction, the converged Hubbard parameters can vary depending on the Hubbard manifolds being considered. In this self-consistent cycle, the parameters from one iteration feed back into the next as a correction term, thereby influencing the KS states and the final converged values. Comparing Figs. 2 and 3 for eACBN0, we find (consistently with LRT) that U_{TM} in CoO increases slightly (by 1–2%), while in FeO it slightly decreases (by 1–4%) in contrast to LRT. For NiO and MnO, U_{TM} exhibits some variations (small increases, decreases, or no significant change), depending on whether the DFT+ U or DFT+ U + V scheme is employed.

The effects of $V_{TM,O}$ and U_O on the magnetic moments are not very significant. The predicted magnetic moments for the TMOs are consistent regardless of computational schemes and they agree well with the experimental range irrespective of inclusion of $V_{TM,O}$. Conversely, the influence of $V_{TM,O}$ is pronounced on the band gap. For eACBN0, the inclusion of $V_{TM,O}$ introduces a non-negligible difference for FeO, CoO and NiO. Nevertheless, the inclusion of U_O has a greater overall impact on the band gap magnitude than $V_{TM,O}$ does. Without U_O (Fig. 2), both methods tend to underestimate the band gaps of MnO and NiO, while results for FeO and CoO are generally in good agreement with experiment. Conversely, including U_O (Fig. 3) increases the band gaps, causing both methods to overestimate them for FeO and CoO. Notably, with U_O , the LRT overestimate the band gaps of FeO, CoO and NiO with and without $V_{TM,O}$. On a material-specific basis, LRT provides a band gap for MnO that is close to the experimental value, whereas eACBN0 still underestimates it. For FeO, CoO and NiO, the trend is reversed: LRT overestimates the gap, while eACBN0 is closer to experiment.

Finally, following the protocol in Fig. S1 in the SI [57], we compute the self-consistent Hubbard parameters and their corresponding optimized structural parameters using both LRT and eACBN0. The results are presented in Fig. S3 and S4 and their discussion is in the SI. For both methods, the structural parameters (lattice constants and rhombohedral angles) are generally in good agreement with available experimental data.

ZrO₂ and BaTiO₃

To further compare the LRT and eACBN0 methods, we examine ZrO₂ and BaTiO₃, where both Zr⁴⁺ and Ti⁴⁺ ions have nominal d^0 electronic configurations. Since these materials are nonmagnetic, the accuracy of the predictions will be assessed based on the band gap as well as the structural properties in the case of BaTiO₃.

Figure 4 shows the results for ZrO₂ without the U_O correction. In LRT, the U parameter for Zr-4d states (U_{Zr}) is ~ 3 eV, reflecting the finite response arising from the small but nonzero occupancy of Zr-4d states in the PBEsol ground state. In contrast, ACBN0, being more

sensitive to the small residual occupancy of the nominal d^0 states, yields a much smaller U_{Zr} value of ~ 0.3 eV, which is one order of magnitude smaller than the LRT value. Consequently, the very small U_{Zr} obtained from ACBN0 leads to a significantly smaller band-gap correction in DFT+ U compared to that obtained using LRT [see Fig. 4(b)].

For the inter-site interactions between Zr-4d and O-2p states ($V_{Zr,O}$), LRT yields values below 1 eV, comparable to those obtained for the TMOs discussed in the previous section. Including these interactions in the DFT+ U + V calculation increases the band gap by 7% relative to DFT+ U with only U_{Zr} from LRT. In contrast, eACBN0 produces substantially larger $V_{Zr,O}$ values (2.3–2.5 eV), leading to a 22% band-gap increase compared to DFT+ U with only U_{Zr} , as shown in Fig. 4(b). Since $V_{Zr,O}$ depends on the interatomic distances between Zr and its nearest-neighbor O atoms, a range of values is reported in Fig. 4(a) rather than a single number. Despite these $V_{Zr,O}$ corrections, both methods still underestimate the experimental band gap by more than 1 eV [91].

Including U_O substantially increases the band gap, as shown in Fig. 5. Both methods (LRT and eACBN0) yield large U_O values in the range of 7–9 eV, with LRT producing the higher values and eACBN0 the lower ones. Incorporating these U_O corrections within either DFT+ U or DFT+ U + V consistently increases the band gap relative to calculations without U_O , bringing the results closer to the experimental value. Overall, LRT-based predictions (whether or not $V_{Zr,O}$ is included) tend to overestimate the band gap, whereas eACBN0-based predictions underestimate it within DFT+ U and slightly overestimate it within DFT+ U + V .

The fully relaxed structures of ZrO₂ are well described by both methods, as shown in Fig. S4, and they are only weakly affected by the inclusion of $V_{Zr,O}$ and U_O . We also note that the method-dependent variations of the “structurally self-consistent” Hubbard parameters during structural relaxation follow the same trends discussed above for the “self-consistent” case at a fixed PBEsol geometry.

Next, we turn to BaTiO₃, which is similar to ZrO₂ in the sense that Ti⁴⁺ also has a nominal d^0 configuration. In this case, we consider not only the band gap but also the crystal-structure properties, which are highly sensitive to Hubbard corrections [61, 92]. BaTiO₃ is a well-known ferroelectric material, exhibiting a rhombohedral distortion at low temperatures. However, standard DFT+ U with sizable U corrections for Ti-3d states incorrectly stabilizes a centrosymmetric cubic structure, thereby suppressing its intrinsic polarization [93]. However, including the inter-site interactions ($V_{Ti,O}$) between Ti-3d and O-2p states preserves their hybridization, which is essential for maintaining the rhombohedral distortion and thus restoring the polarization [61, 92].

In Fig. 6 we present the results obtained using the “self-consistent” scheme described in Fig. 1 without the U_O correction. Within LRT, the Hubbard parameter for

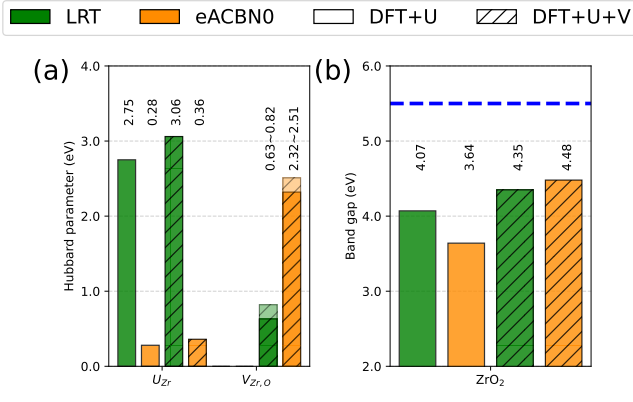


FIG. 4. DFT+U and DFT+U+V self-consistent calculations for ZrO_2 without on-site corrections on O-2p states (U_O). (a) On-site Hubbard U_{Zr} parameter for 4d orbitals of Zr ions and inter-site Hubbard $V_{Zr,O}$ parameter between 4d orbitals of Zr ions and 2p orbitals of oxygen, and (b) band gap. The experimental band gap [91] is shown by the dashed blue line in panel (b).

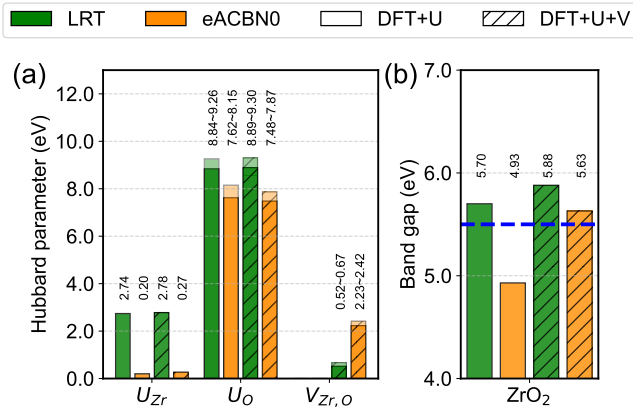


FIG. 5. DFT+U and DFT+U+V self-consistent calculations for ZrO_2 with on-site U_O corrections on O-2p states. The remainder of the caption is analogous to Fig. 4.

the Ti-3d states (U_{Ti}) is ~ 6 eV, reflecting the finite response associated with the small but nonzero 3d occupancy in the PBEsol ground state, similarly to the behavior observed in ZrO_2 . Since Ti-3d states are more localized than Zr-4d states, the resulting U_{Ti} is roughly twice as large as U_{Zr} in LRT. In contrast, ACBN0 yields a very small U_{Ti} of ~ 0.3 eV, identical to U_{Zr} , since the Ti-3d and Zr-4d occupancies are both very low. Thus, ACBN0 appears largely insensitive to the degree of d -state localization (3d vs. 4d), depending primarily on the actual orbital occupancies. As shown in Fig. 6, these differences lead to markedly different DFT+U outcomes: LRT-based DFT+U underestimates the band gap by $\sim 13\%$, whereas eACBN0-based DFT+U underestimates it by $\sim 31\%$. This picture changes substantially when $V_{Ti,O}$ is included. The $V_{Ti,O}$ values obtained from LRT and eACBN0 are similar in magnitude to those found for

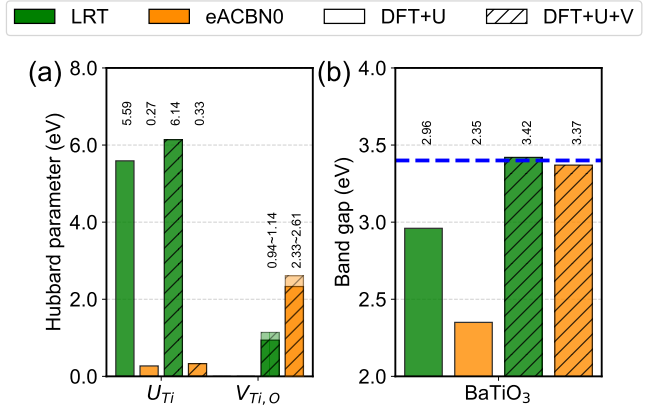


FIG. 6. DFT+U and DFT+U+V self-consistent calculations for BaTiO_3 without on-site corrections on O-2p states (U_O). (a) On-site Hubbard U_{Ti} parameter for 3d orbitals of Ti ions and inter-site Hubbard $V_{Ti,O}$ parameter between 3d orbitals of Ti ions and 2p orbitals of oxygen, and (b) band gap. The experimental band gap [94] is shown by the dashed blue line in panel (b).

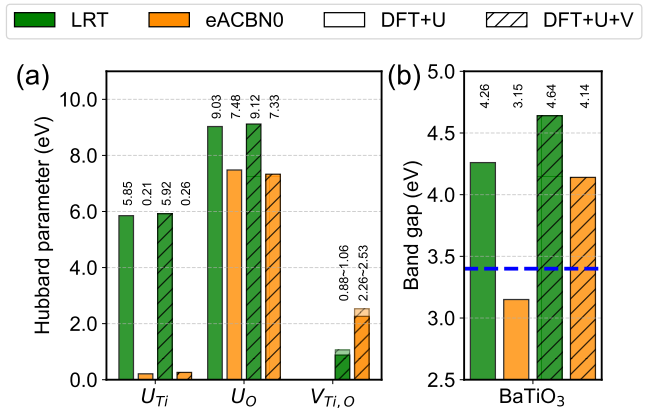


FIG. 7. DFT+U and DFT+U+V self-consistent calculations for BaTiO_3 with on-site U_O corrections on O-2p states. The remainder of the caption is analogous to Fig. 6.

ZrO_2 . With these inter-site interactions included, both methods yield band gaps in excellent agreement with experiment within DFT+U+V. Thus, an accurate band gap is achieved either through a combination of a large U_{Ti} and small $V_{Ti,O}$ (as in LRT) or a small U_{Ti} and large $V_{Ti,O}$ (as in eACBN0).

As shown in Fig. 7(a), the U_O values obtained from LRT and eACBN0 are comparable to those for ZrO_2 (see Fig. 5(a)). Including these U_O corrections has a strong impact on the band gap of BaTiO_3 . In particular, when U corrections are applied to both Ti-3d and O-2p states (and even when the inter-site term $V_{Ti,O}$ is also included) both methods substantially overestimate the band gap (Fig. 7(b)). The only exception is the DFT+U calculation with ACBN0-derived U values, which still underestimates the band gap but by a smaller margin (7%).

Figure S5 in the SI shows the results of the “structurally self-consistent” calculations for BaTiO_3 . The Hubbard parameters U_{Ti} and $V_{Ti,O}$ are only slightly modified compared with those obtained using the PBEsol geometry (compare Fig. S5(c) with Fig. 6(a)). Without U_O , the two methods exhibit different structural trends: LRT-based DFT+ U predicts a cubic phase ($\alpha = 90^\circ$), whereas eACBN0-based DFT+ U retains the rhombohedral distortion ($\alpha < 90^\circ$), as shown in Fig. S5(b). When $V_{Ti,O}$ is included, both methods capture the rhombohedral distortion, but their quantitative predictions differ. Specifically, DFT+ $U+V$ based on LRT parameters yields a lattice parameter, rhombohedral angle, and band gap in very good agreement with experiment, whereas DFT+ $U+V$ based on eACBN0 parameters shows significantly larger deviations for all three properties.

When U_O is included, the structural behavior changes, as shown in Figs. S5(e)–(h). In this case, LRT fails to capture the ferroelectric nature of BaTiO_3 : the large U_{Ti} and U_O values overly localize the $\text{Ti-}3d$ and $\text{O-}2p$ states, respectively, driving the system into a non-polar cubic phase even when the small inter-site interaction $V_{Ti,O}$ is added (Fig. S5(f)). A similar trend occurs in eACBN0-based DFT+ U calculations, where the combined inclusion of small U_{Ti} and large U_O suppresses the polarization and restores cubic symmetry. However, unlike LRT, adding large $V_{Ti,O}$ within the eACBN0 framework recovers the rhombohedral distortion and the associated polarization, consistent with previous findings [92]. Nonetheless, the resulting lattice parameter and band gap remain substantially overestimated.

These results highlight that, although both approaches rely on similar Hubbard correction schemes, they lead to qualitatively different effects on structural and electronic properties of BaTiO_3 . Namely, LRT yields the most accurate properties when U_{Ti} and $V_{Ti,O}$ are included but U_O is excluded, whereas eACBN0 achieves its best accuracy when all correction terms are included.

ZnO

After examining TMOs with partially filled d states (from Mn^{2+} to Ni^{2+}) and then early TM compounds with nominal d^0 configurations (Ti^{4+} and Zr^{4+}), we now turn to a material with a late d -block element: ZnO, where Zn^{2+} has a nominally filled d^{10} configuration. ZnO represents the opposite extreme of the d -electron occupancy spectrum relative to the d^0 systems, offering a distinctly different test case for evaluating Hubbard parameters.

We first discuss the results for ZnO without the U_O correction. As shown in Fig. 8, the LRT method yields an unphysically large self-consistent U_{Zn} exceeding 100 eV. Even without performing the full self-consistent cycle (see Fig. 1), i.e. using the “one-shot” scheme, the LRT estimate already exceeds 25 eV. This well-known limitation of LRT arises from the fully occupied Zn-3d shell, which leads to spuriously large U values [90]. The “structurally

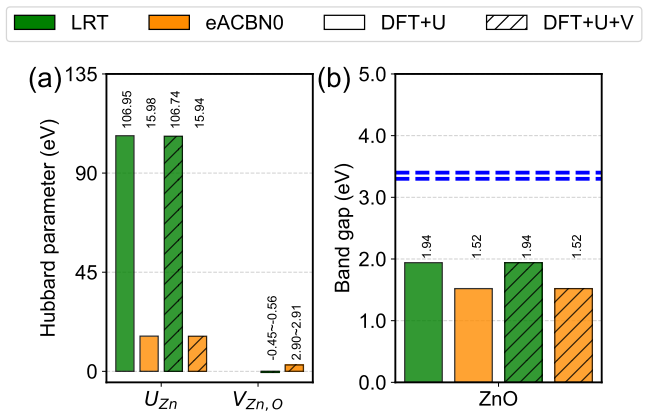


FIG. 8. DFT+ U and DFT+ $U+V$ self-consistent calculations for ZnO without on-site corrections on O-2p states (U_O). (a) On-site Hubbard U_{Zn} parameter for 3d orbitals of Zn ions and inter-site Hubbard $V_{Zn,O}$ parameter between 3d orbitals of Zn ions and 2p orbitals of oxygen, and (b) band gap. The experimental band gap [95–98] is shown by the dashed blue lines in panel (b).

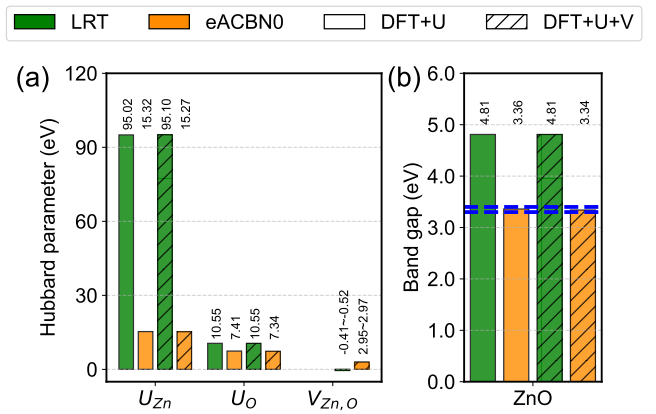


FIG. 9. DFT+ U and DFT+ $U+V$ self-consistent calculations for ZnO with on-site U_O corrections on O-2p states. The remainder of the caption is analogous to Fig. 8.

self-consistent” scheme produces a similarly large U_{Zn} , as shown in Fig. S6. It is important to emphasize that in ZnO the valence-band maximum is primarily O-2p in character, while the conduction-band minimum is dominated by Zn-4s states. As a result, applying U_{Zn} to the Zn-3d states influences the band gap only indirectly. Indeed, LRT-based DFT+ U increases the PBEsol band gap from ~ 0.7 eV to 1.94 eV, which remains well below the experimental value of $3.3 \sim 3.4$ eV [95–98]. In contrast, the eACBN0 approach predicts also large but more moderate U_{Zn} of ~ 16 eV, resulting in a slightly smaller band gap of 1.52 eV, as shown in Fig. 8(b).

For the inter-site interactions between Zn-3d and O-2p states ($V_{Zn,O}$), LRT yields small negative values. These unphysical negative values likely originate from numerical instabilities during the inversion of response matrices

whose elements are close to zero and therefore highly sensitive to numerical noise. In contrast, eACBN0 produces significantly larger and more stable $V_{Zn,O}$ values of about 3 eV, consistently with the trends observed for the other materials discussed above. However, these inter-site corrections have no effect on the band gap, as shown in Fig. 8(b). This insensitivity arises because the band gap in ZnO is defined between O-2p (valence) and Zn-4s (conduction) states, while the Zn-3d states lie much deeper in energy. As a result, the $V_{Zn,O}$ term mainly alters the hybridization between the O-2p and Zn-3d states but does not influence the band edges, leaving the band gap unchanged.

Including U_O in addition to U_{Zn} , as shown in Fig. 9, leads to markedly different outcomes. In LRT, the already unphysical U_{Zn} value combined with a large $U_O \sim 11$ eV results in a band gap that overestimates the experimental value by 44%. In contrast, eACBN0 yields still large but more moderate values, $U_{Zn} \sim 15$ eV and $U_O \sim 7$ eV, which together produce a band gap in excellent agreement with experiment. As before, adding the inter-site term $V_{Zn,O}$ has no influence on the band gap for the reasons discussed above. These results show that the band gap is highly sensitive to U_O , since this correction directly shifts the O-2p states that form the valence-band maximum in ZnO.

When structural relaxations are included, both the Hubbard parameters and the resulting band gaps follow similar trends as described above (see Fig. S6). We also note that, with these Hubbard corrections, both methods reproduce the experimental structural parameters very well (see Fig. S6(a) and (d)).

DISCUSSION

Based on the numerical results presented in the previous section, we now provide a discussion and interpretation of the observed trends in the behavior of the on-site U and inter-site V Hubbard parameters obtained from LRT and eACBN0. Despite the fundamentally different mathematical formulations and physical concepts underlying these two methods, there are cases where they yield comparable U values, as well as cases where the results diverge dramatically. By contrast, the inter-site V parameters systematically exhibit large discrepancies between the two approaches. In what follows, we analyze these similarities and differences in more detail.

We start with the on-site U_{TM} values. For TMOs with partially occupied 3d shells, LRT and eACBN0 predict similar U_{TM} values except U for Fe in FeO that differs by 2–3 eV. However, when the 3d shell is nearly empty or fully occupied, the two methods behave in fundamentally different ways. In particular, for nominally empty 3d states, LRT still produces finite and sizable U_{TM} values in the range of 3–6 eV, while for fully occupied 3d states it yields unphysically large values. The latter is a well-known limitation of the LRT framework [90]: for

filled shells, the occupation matrices exhibit vanishing variations under a local electronic perturbation, leading to nearly singular response matrices whose inversion generates spuriously large U_{TM} values. The behavior of eACBN0 is markedly different: It produces U_{TM} values that are finite and in the range of physical values even for closed shells. The root cause of this behavior lies in the definition of the auxiliary objects - the renormalized occupation numbers [Eq. (13)] and renormalized density matrices [Eq. (12)]. These quantities are constructed to ensure that the sum of the Mulliken charge of each atom and the interatomic charge reproduces the correct total electronic population. As a consequence, the Hubbard parameters derived from eACBN0 naturally become very small for nearly empty shells, while for fully filled 3d shells they approach values of ~ 16 eV. This trend is not mirrored in LRT because of the different physical idea: U_{TM} is computed from the occupation-matrix variations in response to local electronic perturbations. For nearly empty shells, even an infinitesimal local perturbation can induce relatively large fractional changes in the occupation matrix, which translates into sizable U_{TM} values. Conversely, for fully occupied shells, the occupation matrix is extremely rigid, and the small changes captured by the linear-response equations produce nearly vanishing matrix elements. The inversion of these nearly singular matrices amplifies the response artificially, resulting in unphysically large U_{TM} values. Thus, while LRT and eACBN0 can yield comparable results for partially filled shells, their behavior diverges sharply at the two extremes of the d -electron occupation spectrum.

Regarding the on-site Hubbard U_O parameter for O-2p states, as obtained from LRT and eACBN0, we observe notable differences. On the one hand, LRT consistently predicts large U_O values, close to 10 eV, essentially independent of the specific compound under investigation. This apparent universality suggests that in LRT the variation of the occupation matrix for O-2p states is very similar across materials, regardless of their degree of localization or hybridization. In contrast, the eACBN0 approach provides a much broader and more system-dependent distribution of U_O values, ranging from 2 to 8 eV. Specifically, U_O is about 2–3 eV for TMOs, but increases to 7–8 eV in ZnO, ZrO_2 and $BaTiO_3$. These results indicate that the U_O value does not follow the same systematic trend as the U_{TM} values, which generally scale with the electron count. This behavior can be rationalized by considering that the degree of localization and hybridization of O-2p states varies strongly across materials. In some cases, such as in ZrO_2 and $BaTiO_3$, the oxygen states are more localized, resulting in larger U_O values. Additionally, it is important to account for the fact that O-2p states participate in significant charge redistribution and hybridization with TM-3d. This naturally calls for the inclusion of inter-site V terms in order to properly capture the covalency of such interactions, since purely on-site corrections are insufficient to describe the entangled nature of oxygen states.

Next, we turn to the inter-site V interactions between TM- d and O- p states in the studied materials. From our LRT calculations, we find that for all compounds except ZnO, V values are typically around 1 eV or smaller, while in ZnO they are small and negative. Such values are characteristic of LRT: V corresponds to the off-diagonal elements of the response matrix, describing how the occupation on a given atom changes when a neighboring atom is perturbed. Since these inter-site responses are much weaker than the on-site ones (which define U), the resulting V is generally small. In ZnO, the small negative V originates from numerical instabilities caused by inverting nearly singular response matrices. In contrast, eACBN0 yields a markedly different picture: The inter-site V values are much larger, often comparable in magnitude to the on-site U . For instance, in TMOs with partially occupied 3d shells and in ZnO, V is 2–5 times smaller than the corresponding U_{TM} . Even more strikingly, in ZrO₂ and BaTiO₃, V exceeds the U_{TM} values of the nominally empty d states by a factor of ~ 10 . This behavior stems from the fact that in eACBN0, the formation of a chemical bond involves charge redistribution between atoms, placing U and V on a more equal footing than in LRT. Indeed, Eq. (13) shows that V^{IJ} scales with the sum of Mulliken charges of atoms I and J , and is therefore not intrinsically smaller than its on-site counterpart. Moreover, since eACBN0 derives U and V from energy contributions that depend on the spatial distribution of electronic charges, bonding tends to lower on-site U while enhancing inter-site V . In this framework, the ratio U/V reflects the balance between atomic and bond-centered charges, and is thus directly tied to bond strength. Consequently, V remains sizable relative to U in all systems. By contrast, in LRT the U and V parameters emerge from occupation matrix responses, where the dominant contribution is always local. As a result, U is much larger than V , with ratios often an order of magnitude.

In summary, we have carried out a systematic comparison of two widely used approaches, LRT and eACBN0, for computing on-site U and inter-site V Hubbard parameters across three classes of materials spanning nearly empty, partially filled, and fully occupied TM- d shells. These two methods rest on fundamentally different physical pictures and mathematical frameworks, yet our analysis reveals both points of agreement and distinct discrepancies. For TMOs with partially occupied d states, the two methods yield broadly consistent U values, whereas for nearly empty or fully filled d shells the disagreement becomes substantial, reflecting intrinsic differences in how each method treats electronic interactions. For the O-2p states, LRT systematically predicts large U values independent of chemistry, while eACBN0 produces a much wider spread, sensitive to localization and hybridization with TM- d states. The contrast is even sharper for the inter-site V : LRT consistently yields small values (~ 1 eV or less), while eACBN0 predicts much larger values, often comparable to on-site U . These

differences can be traced to the distinct mathematical assumptions underpinning the definitions of U and V , and to the different physical insights each method encodes - LRT focusing on response functions, eACBN0 on energetics and charge redistribution. Overall, our study highlights that while certain parallels exist for the considered set of materials, the divergences between LRT and eACBN0 are pronounced and can affect the predicted material properties for specific cases. This work represents a first step toward a systematic understanding of how these methods compare and where they diverge. Bridging their conceptual and mathematical foundations, and testing them across a broader range of materials and chemistry, remains an important direction for future developments.

METHODS

All calculations were performed using the plane-wave pseudopotential method as implemented in the QUANTUM ESPRESSO (QE) distribution [99–101]. For the xc functional, we adopted the σ -GGA with the PBEsol parametrization [102], and used pseudopotentials from the GBRV library (v1.5) [103]. The KS wavefunctions and potentials were expanded in plane waves with kinetic-energy cutoffs of 65 and 780 Ry for the TMOs, and 60 and 600 Ry for ZnO, ZrO₂, and BaTiO₃. The first BZ was sampled using uniform Γ -centered \mathbf{k} -point meshes: $10 \times 10 \times 10$ for TMOs, $12 \times 12 \times 7$ for ZnO, $7 \times 7 \times 6$ for ZrO₂, and $8 \times 8 \times 8$ for BaTiO₃. Spin-orbit coupling was neglected. Geometry optimizations were carried out using the Broyden–Fletcher–Goldfarb–Shanno (BFGS) algorithm [104], with convergence criteria of 10^{-4} Ry for the total energy, 10^{-3} Ry/Bohr for forces, and 0.5 kbar for pressure in TMOs. For ZnO, ZrO₂, and BaTiO₃, criteria of 10^{-6} Ry for the total energy, 10^{-5} Ry/Bohr for forces, and 0.5 kbar for pressure were adopted.

The LRT Hubbard parameters were computed using DFPT [56, 57] as implemented in the HP code [105]. Hubbard projectors were constructed from atomic orbitals orthogonalized using the Löwdin scheme [71]. Uniform Γ -centered \mathbf{k} - and \mathbf{q} -point grids were employed, with sizes of $10 \times 10 \times 10$ and $6 \times 6 \times 6$ for TMOs, $12 \times 12 \times 7$ and $6 \times 6 \times 3$ for ZnO, $7 \times 7 \times 6$ and $3 \times 3 \times 3$ for ZrO₂, and $8 \times 8 \times 8$ and $4 \times 4 \times 4$ for BaTiO₃, respectively.

The eACBN0 Hubbard parameters were computed using our modified in-house QE package [44, 66]. For consistency with the LRT approach, the Hubbard projectors were constructed from atomic orbitals orthogonalized using the Löwdin scheme [71]. The same Γ -centered \mathbf{k} -point meshes used for the electronic structure calculations were employed, and convergence thresholds of 10^{-10} and 10^{-15} Ry were applied for the total eACBN0 energy and SCF cycle, respectively.

The U and V parameters were obtained using two self-consistent protocols, summarized in Fig. 1 and Fig. S1 of the SI. In the main text, we report the values computed

by iteratively evaluating U and V on the PBEsol-relaxed structures using the LRT and eACBN0 methods until convergence (the “self-consistent” scheme). In the case of ZnO, however, this iterative procedure was limited to two steps due to its tendency to diverge [90]. For completeness, the SI also presents results from the “structurally self-consistent” scheme, in which DFT+ U + V structural optimizations (including Hubbard contributions to forces and stresses [106]) are performed, and the Hubbard parameters are recomputed until both the structure and the U and V values are converged.

DATA AVAILABILITY

The data used to produce the results of this work will be available in the Materials Cloud Archive. Our modi-

fied in-house QE code for eACBN0 calculations is available at <https://github.com/KIAS-CMT/DFT-U-V>.

ACKNOWLEDGEMENTS

W.Y. was supported by KIAS individual Grant (No. QP090102). I.T. acknowledges support from the Swiss National Science Foundation (Grant No. 200021-227641 and No. 200021-236507). Y.-W.S. was supported by KIAS individual Grant (No. CG031509). Computer time was provided by the Swiss National Supercomputing Centre (CSCS) under project No. s1073, lp18, s1326, and the CAC of KIAS.

[1] P. Hohenberg and W. Kohn, Inhomogeneous electron gas, *Phys. Rev.* **136**, B864 (1964).

[2] W. Kohn and L. Sham, Self-consistent equations including exchange and correlation effects, *Phys. Rev.* **140**, A1133 (1965).

[3] J. Perdew and A. Zunger, Self-interaction correction to density-functional approximations for many-electron systems, *Phys. Rev. B* **23**, 5048 (1981).

[4] P. Mori-Sánchez, A. Cohen, and W. Yang, Many-electron self-interaction error in approximate density functionals, *J. Chem. Phys.* **125**, 201102 (2006).

[5] V. Anisimov, J. Zaanen, and O. Andersen, Band theory and Mott insulators: Hubbard U instead of Stoner I , *Phys. Rev. B* **44**, 943 (1991).

[6] A. Liechtenstein, V. Anisimov, and J. Zaanen, Density-functional theory and strong interactions: Orbital ordering in Mott-Hubbard insulators, *Phys. Rev. B* **52**, R5467 (1995).

[7] S. Dudarev, G. Botton, S. Savrasov, C. Humphreys, and A. Sutton, Electron-energy-loss spectra and the structural stability of nickel oxide: An LSDA+ U study, *Phys. Rev. B* **57**, 1505 (1998).

[8] V. L. Campo Jr and M. Cococcioni, Extended DFT+ U + V method with on-site and inter-site electronic interactions, *J. Phys.: Condens. Matter* **22**, 055602 (2010).

[9] J. Sun, A. Ruzsinszky, and J. Perdew, Strongly Constrained and Appropriately Normed Semilocal Density Functional, *Phys. Rev. Lett.* **115**, 036402 (2015).

[10] A. Bartók and J. Yates, Regularized SCAN functional, *J. Chem. Phys.* **150**, 161101 (2019).

[11] J. Furness, A. Kaplan, J. Ning, J. Perdew, and J. Sun, Accurate and Numerically Efficient r^2 SCAN Meta-Generalized Gradient Approximation, *J. Phys. Chem. Lett.* **11**, 8208 (2020).

[12] C. Adamo and V. Barone, Toward reliable density functional methods without adjustable parameters: The PBE0 model, *J. Chem. Phys.* **110**, 6158 (1999).

[13] J. Heyd, G. Scuseria, and M. Ernzerhof, Hybrid functionals based on a screened Coulomb potential, *J. Chem. Phys.* **118**, 8207 (2003).

[14] J. Heyd, G. Scuseria, and M. Ernzerhof, Erratum: “Hybrid functionals based on a screened Coulomb potential” [J. Chem. Phys. 118, 8207 (2003)], *J. Chem. Phys.* **124**, 219906 (2006).

[15] G. Gautam and E. Carter, Evaluating transition metal oxides within DFT-SCAN and SCAN+ U frameworks for solar thermochemical applications, *Phys. Rev. Materials* **2**, 095401 (2018).

[16] O. Long, G. Gautam, and E. Carter, Evaluating optimal U for 3d transition-metal oxides within the SCAN+ U framework, *Phys. Rev. Materials* **4**, 045401 (2020).

[17] J. Kaczkowski, M. Pugaczowa-Michalska, and I. Płowaś-Korus, Comparative density functional studies of pristine and doped bismuth ferrite polymorphs by GGA+ U and meta-GGA SCAN+ U , *Phys. Chem. Chem. Phys.* **23**, 8571 (2021).

[18] N. Artrith, J. Torres, A. Urban, and M. Hybertsen, Data-driven approach to parameterize SCAN+ U for an accurate description of 3d transition metal oxide thermochemistry, *Phys. Rev. Materials* **6**, 035003 (2022).

[19] H. Kulik, M. Cococcioni, D. Scherlis, and N. Marzari, Density Functional Theory in Transition-Metal Chemistry: A Self-Consistent Hubbard U Approach, *Phys. Rev. Lett.* **97**, 103001 (2006).

[20] H. Kulik and N. Marzari, A self-consistent Hubbard U density-functional theory approach to the addition-elimination reactions of hydrocarbons on bare FeO^+ , *J. Chem. Phys.* **129**, 134314 (2008).

[21] I. Timrov, F. Aquilante, M. Cococcioni, and N. Marzari, Accurate Electronic Properties and Intercalation Voltages of Olivine-type Li-ion Cathode Materials from Extended Hubbard Functionals, *PRX Energy* **1**, 033003 (2022).

[22] B. Hımmetoglu, A. Floris, S. de Gironcoli, and M. Cococcioni, Hubbard-corrected DFT energy functionals: The LDA+ U description of correlated systems, *Int. J. Quant. Chem.* **114**, 14 (2014).

[23] L. Hedin, New Method for Calculating the One-Particle Green’s Function with Application to the Electron-Gas Problem, *Phys. Rev.* **139**, A796 (1965).

[24] L. Wang, T. Maxisch, and G. Ceder, Oxidation energies of transition metal oxides within the GGA+U framework, *Phys. Rev. B* **73**, 195107 (2006).

[25] O. Kubaschewski, C. Alcock, and P. Spencer, *Materials thermochemistry*, 6th ed. (Pergamon Press: Elmsford, New York, 1993).

[26] O. Le Bacq, A. Pasturel, and O. Bengone, Impact on electronic correlations on the structural stability, magnetism, and voltage of LiCoPO₄ battery, *Phys. Rev. B* **69**, 245107 (2004).

[27] M. Aykol and C. Wolverton, Local environment dependent GGA+U method for accurate thermochemistry of transition metal compounds, *Phys. Rev. B* **90**, 115105 (2014).

[28] E. Isaacs and C. Marianetti, Compositional phase stability of strongly correlated electron materials within DFT+U, *Phys. Rev. B* **95**, 045141 (2017).

[29] M. Yu, S. Yang, C. Wu, and N. Marom, Machine learning the Hubbard U parameter in DFT+U using Bayesian optimization, *npj Comput. Mater.* **6**, 180 (2020).

[30] P. Tavadze, R. Boucher, G. Avendano-Franco, K. Kocan, S. Singh, V. Dovale-Farelo, W. Ibarra-Hernández, M. Johnson, D. Mebane, and A. Romero, Exploring DFT+U parameter space with a Bayesian calibration assisted by Markov chain Monte Carlo sampling, *npj Comput. Mater.* **7**, 182 (2021).

[31] P. Dederichs, S. Blügel, R. Zeller, and H. Akai, Ground States of Constrained Systems: Application to Cerium Impurities, *Phys. Rev. Lett.* **53**, 2512 (1984).

[32] A. McMahan, R. Martin, and S. Satpathy, Calculated effective Hamiltonian for La₂CuO₄ and solution in the impurity Anderson approximation, *Phys. Rev. B* **38**, 6650 (1988).

[33] O. Gunnarsson, O. Andersen, O. Jepsen, and J. Zaanen, Density-functional calculation of the parameters in the Anderson model: Application to Mn in CdTe, *Phys. Rev. B* **39**, 1708 (1989).

[34] M. Hybertsen, M. Schlüter, and N. Christensen, Calculation of Coulomb-interaction parameters for La₂CuO₄ using a constrained-density-functional approach, *Phys. Rev. B* **39**, 9028 (1989).

[35] O. Gunnarsson, Calculation of parameters in model Hamiltonians, *Phys. Rev. B* **41**, 514 (1990).

[36] W. Pickett, S. Erwin, and E. Ethridge, Reformulation of the LDA+U method for a local-orbital basis, *Phys. Rev. B* **58**, 1201 (1998).

[37] I. Solovyev and M. Imada, Screening of Coulomb interactions in transition metals, *Phys. Rev. B* **71**, 045103 (2005).

[38] K. Nakamura, R. Arita, Y. Yoshimoto, and S. Tsuneyuki, First-principles calculation of effective onsite Coulomb interactions of 3d transition metals: Constrained local density functional approach with maximally localized Wannier functions, *Phys. Rev. B* **74**, 235113 (2006).

[39] M. Shishkin and H. Sato, Self-consistent parametrization of DFT+U framework using linear response approach: Application to evaluation of redox potentials of battery cathodes, *Phys. Rev. B* **93**, 085135 (2016).

[40] N. Mosey and E. Carter, Ab initio evaluation of Coulomb and exchange parameters for DFT+U calculations, *Phys. Rev. B* **76**, 155123 (2007).

[41] N. Mosey, P. Liao, and E. Carter, Rotationally invariant ab initio evaluation of Coulomb and exchange parameters for DFT+U calculations, *J. Chem. Phys.* **129**, 014103 (2008).

[42] A. Andriotis, R. Sheetz, and M. Menon, LSDA+U method: A calculation of the U values at the Hartree-Fock level of approximation, *Phys. Rev. B* **81**, 245103 (2010).

[43] L. Agapito, S. Curtarolo, and M. Buongiorno Nardelli, Reformulation of DFT+U as a Pseudohybrid Hubbard Density Functional for Accelerated Materials Discovery, *Phys. Rev. X* **5**, 011006 (2015).

[44] S.-H. Lee and Y.-W. Son, First-principles approach with a pseudohybrid density functional for extended Hubbard interactions, *Phys. Rev. Research* **2**, 043410 (2020).

[45] N. Tancogne-Dejean and A. Rubio, Parameter-free hybridlike functional based on an extended Hubbard model: DFT+U+V, *Phys. Rev. B* **102**, 155117 (2020).

[46] M. Springer and F. Aryasetiawan, Frequency-dependent screened interaction in Ni within the random-phase approximation, *Phys. Rev. B* **57**, 4364 (1998).

[47] T. Kotani, *Ab initio* random-phase-approximation calculation of the frequency-dependent effective interaction between 3d electrons: Ni, Fe, and MnO, *J. Phys.: Condens. Matter* **12**, 2413 (2000).

[48] F. Aryasetiawan, M. Imada, A. Georges, G. Kotliar, S. Biermann, and A. Lichtenstein, Frequency-dependent local interactions and low-energy effective models from electronic structure calculations, *Phys. Rev. B* **70**, 195104 (2004).

[49] F. Aryasetiawan, K. Karlsson, O. Jepsen, and U. Scönberger, Calculations of Hubbard U from first-principles, *Phys. Rev. B* **74**, 125106 (2006).

[50] B.-L. Liu, Y.-C. Wang, Y. Liu, Y.-J. Xu, X. Chen, H.-Z. Song, Y. Bi, H.-F. Liu, and H.-F. Song, Comparative study of first-principles approaches for effective Coulomb interaction strength U_{eff} between localized f -electrons: Lanthanide metals as an example, *J. Chem. Phys.* **158**, 084108 (2023).

[51] A. Carta, I. Timrov, S. Beck, and C. Ederer, Bridging constrained random-phase approximation and linear response theory for computing Hubbard parameters, *arXiv:2505.03698* (2025).

[52] R. Mahajan, I. Timrov, N. Marzari, and A. Kashyap, Importance of intersite Hubbard interactions in β -MnO₂: A first-principles DFT+U+V study, *Phys. Rev. Materials* **5**, 104402 (2021).

[53] The selection of a specific first-principles method to compute U can be influenced by the intended applications and the properties of interest. Notably, cRPA is the preferred method for determining U in the context of subsequent DFT plus dynamical mean field theory (DFT+DMFT) calculations [?].

[54] M. Cococcioni and S. de Gironcoli, Linear response approach to the calculation of the effective interaction parameters in the LDA+U method, *Phys. Rev. B* **71**, 035105 (2005).

[55] B. Himmetoglu, R. Wentzcovitch, and M. Cococcioni, *Phys. Rev. B* **84**, 115108 (2011).

[56] I. Timrov, N. Marzari, and M. Cococcioni, Hubbard parameters from density-functional perturbation theory, *Phys. Rev. B* **98**, 085127 (2018).

[57] I. Timrov, N. Marzari, and M. Cococcioni, Self-consistent Hubbard parameters from density-functional perturbation theory in the ultrasoft and projector-augmented wave formulations, *Phys. Rev. B* **103**, 045141 (2021).

[58] R. Mahajan, A. Kashyap, and I. Timrov, Pivotal Role of Intersite Hubbard Interactions in Fe-Doped α -MnO₂, *J. Phys. Chem. C* **126**, 14353 (2022).

[59] I. Timrov, M. Kotiuga, and N. Marzari, Unraveling the effects of inter-site Hubbard interactions in spinel Li-ion cathode materials, *Phys. Chem. Chem. Phys.* **25**, 9061 (2023).

[60] L. Binci, M. Kotiuga, I. Timrov, and N. Marzari, Hybridization driving distortions and multiferroicity in rare-earth nickelates, *Phys. Rev. Research* **5**, 033146 (2023).

[61] G. Gebreyesus, L. Bastonero, M. Kotiuga, N. Marzari, and **I. Timrov**, Understanding the role of Hubbard corrections in the rhombohedral phase of BaTiO₃, *Phys. Rev. B* **108**, 235171 (2023).

[62] F. Haddadi, E. Linscott, I. Timrov, N. Marzari, and M. Gibertini, On-site and inter-site Hubbard corrections in magnetic monolayers: The case of FePS₃ and CrI₃, *Phys. Rev. Materials* **8**, 014007 (2024).

[63] P. Bonfá, I. Onuorah, F. Lang, I. Timrov, L. Monacelli, C. Wang, X. Sun, O. Petracic, G. Pizzi, N. Marzari, S. Blundell, and R. De Renzi, Magnetostriction-driven muon localisation in an antiferromagnetic oxide, *Phys. Rev. Lett.* **132**, 046701 (2024).

[64] E. Macke, I. Timrov, N. Marzari, and L. C. Ciacchi, Orbital-Resolved DFT+U for Molecules and Solids, *J. Chem. Theory Comput.* **20**, 4824 (2024).

[65] K. Warda, E. Macke, I. Timrov, L. Ciacchi, and P. Kowalski, Getting the manifold right: The crucial role of orbital resolution in DFT+U for mixed *d-f* electron compounds, [arXiv:2508.16435](https://arxiv.org/abs/2508.16435) (2025).

[66] W. Yang, S.-H. Jhi, S.-H. Lee, and Y.-W. Son, Ab initio study of lattice dynamics of group iv semiconductors using pseudohybrid functionals for extended hubbard interactions, *Phys. Rev. B* **104**, 104313 (2021).

[67] W. Yang, B. G. Jang, Y.-W. Son, and S.-H. Jhi, Lattice dynamical properties of antiferromagnetic oxides calculated using self-consistent extended hubbard functional method, *Journal of Physics: Condensed Matter* **34**, 295601 (2022).

[68] B. G. Jang, M. Kim, S.-H. Lee, W. Yang, S.-H. Jhi, and Y.-W. Son, Intersite coulomb interactions in charge-ordered systems, *Phys. Rev. Lett.* **130**, 136401 (2023).

[69] W. Yang, S. Tiwari, F. Giustino, and Y.-W. Son, First-principles electron-phonon interactions with self-consistent hubbard interaction: Application to transparent conducting oxides, *Phys. Rev. B* **112**, 075203 (2025).

[70] N. Kirchner-Hall, W. Zhao, Y. Xiong, I. Timrov, and I. Dabo, Extensive Benchmarking of DFT+U Calculations for Predicting Band Gaps, *Appl. Sci.* **11**, 2395 (2021).

[71] P.-O. Löwdin, On the Non-Orthogonality Problem Connected with the Use of Atomic Wave Functions in the Theory of Molecules and Crystals, *J. Chem. Phys.* **18**, 365 (1950).

[72] I. Mayer, On Löwdin's method of symmetric orthogonalization, *Int. J. Quant. Chem.* **90**, 63 (2002).

[73] S. Gelin, N. Kirchner-Hall, R. Katzbaer, M. Theibault, Y. Xiong, W. Zhao, M. Khan, E. Andrewlavage, P. Orbe, S. Baksa, M. Cococcioni, I. Timrov, Q. Campbell, H. Abruna, R. Schaak, and I. Dabo, Ternary oxides of *s*- and *p*-block metals for photocatalytic solar-to-hydrogen conversion, *PRX Energy* **3**, 013007 (2024).

[74] M. Uhrin, A. Zadoks, L. Binci, N. Marzari, and I. Timrov, Machine learning Hubbard parameters with equivariant neural networks, *npj Comput. Mater.* **11**, 19 (2025).

[75] L. Bastonero, C. Malica, E. Macke, M. Bercx, I. T. S. Huber, and N. Marzari, First-principles Hubbard parameters with automated and reproducible workflows, *npj Comput. Mater.* **11**, 183 (2025).

[76] B. Chang, **I. Timrov**, J. Park, J.-J. Zhou, N. Marzari, and M. Bernardi, First-principles electron-phonon interactions and polarons in the parent cuprate La₂CuO₄, *Phys. Rev. Research* **7**, L012073 (2025).

[77] L. Binci, N. Marzari, and I. Timrov, Magnons from time-dependent density-functional perturbation theory and nonempirical Hubbard functionals, *npj Comput. Mater.* **11**, 100 (2025).

[78] F. dos Santos, L. Binci, G. Menichetti, R. Mahajan, N. Marzari, and I. Timrov, Comparative study of magnetic exchange parameters and magnon dispersions in NiO and MnO from first principles, [arXiv:2508.12153](https://arxiv.org/abs/2508.12153) (2025).

[79] E. Z. Kurmaev, R. G. Wilks, A. Moewes, L. D. Finkelstein, S. N. Shamin, and J. Kuneš, Oxygen x-ray emission and absorption spectra as a probe of the electronic structure of strongly correlated oxides, *Phys. Rev. B* **77**, 165127 (2008).

[80] J. van Elp, R. H. Potze, H. Eskes, R. Berger, and G. A. Sawatzky, Electronic structure of mno, *Phys. Rev. B* **44**, 1530 (1991).

[81] A. K. Cheetham and D. A. O. Hope, Magnetic ordering and exchange effects in the antiferromagnetic solid solutions $mn_xni_{1-x}O$, *Phys. Rev. B* **27**, 6964 (1983).

[82] B. E. F. Fender, A. J. Jacobson, and F. A. Wedgwood, Covalency parameters in mno, α -mns, and nio, *The Journal of Chemical Physics* **48**, 990 (1968).

[83] H. Bowen, D. Adler, and B. Auker, Electrical and optical properties of feo, *Journal of Solid State Chemistry* **12**, 355 (1975).

[84] W. L. Roth, Magnetic structures of mno, feo, coo, and nio, *Phys. Rev.* **110**, 1333 (1958).

[85] P. Battle and A. Cheetham, The magnetic structure of non-stoichiometric ferrous oxide, *Journal of Physics C: Solid State Physics* **12**, 337 (1979).

[86] J. van Elp, J. L. Wieland, H. Eskes, P. Kuiper, G. A. Sawatzky, F. M. F. de Groot, and T. S. Turner, Electronic structure of coo, li-doped coo, and licoo₂, *Phys. Rev. B* **44**, 6090 (1991).

[87] D. C. Khan and R. A. Erickson, Magnetic form factor of co⁺⁺ ion in cobaltous oxide, *Phys. Rev. B* **1**, 2243 (1970).

[88] W. Jauch, M. Reehuis, H. J. Bleif, F. Kubanek, and P. Pattison, Crystallographic symmetry and magnetic structure of coo, *Phys. Rev. B* **64**, 052102 (2001).

[89] G. A. Sawatzky and J. W. Allen, Magnitude and origin of the band gap in nio, *Phys. Rev. Lett.* **53**, 2339 (1984).

[90] K. Yu and E. Carter, Comparing ab initio methods of obtaining effective *u* parameters for closed-shell materials, *J. Chem. Phys.* **140**, 121105 (2014).

[91] E. Bersch, S. Rangan, R. A. Bartynski, E. Garfunkel, and E. Vescovo, Band offsets of ultrathin high- κ oxide films with si, *Phys. Rev. B* **78**, 085114 (2008).

[92] M. C. Choi, W. Yang, Y.-W. Son, and S. Y. Park, First-principles study of dielectric properties of ferroelectric perovskite oxides with on-site and inter-site hubbard interactions, *npj Comput. Mater.* **11**, 221 (2025).

[93] N. Tsunoda, Y. Kumagai, and F. Oba, Stabilization of small polarons in BaTi_3 by local distortions, *Phys. Rev. Mater.* **3**, 114602 (2019).

[94] S. H. Wemple, Polarization fluctuations and the optical-absorption edge in BaTi_3 , *Phys. Rev. B* **2**, 2679 (1970).

[95] A. Mang, K. Reimann, and S. Rübenacke, Band gaps, crystal-field splitting, spin-orbit coupling, and exciton binding energies in ZnO under hydrostatic pressure, *Solid State Commun.* **94**, 251 (1995).

[96] Y. Chen, D. M. Bagnall, H.-j. Koh, K.-t. Park, K. Hiraga, Z. Zhu, and T. Yao, Plasma assisted molecular beam epitaxy of ZnO on *c*-plane sapphire: Growth and characterization, *J. Appl. Phys.* **84**, 3912 (1998), https://pubs.aip.org/aip/jap/article-pdf/84/7/3912/19186519/3912_1.online.pdf.

[97] D. C. Reynolds, D. C. Look, B. Jogai, C. W. Litton, G. Cantwell, and W. C. Harsch, Valence-band ordering in ZnO , *Phys. Rev. B* **60**, 2340 (1999).

[98] C. L. Dong, C. Persson, L. Vayssieres, A. Augustsson, T. Schmitt, M. Mattesini, R. Ahuja, C. L. Chang, and J.-H. Guo, Electronic structure of nanostructured ZnO from x-ray absorption and emission spectroscopy and the local density approximation, *Phys. Rev. B* **70**, 195325 (2004).

[99] P. Giannozzi, S. Baroni, N. Bonini, M. Calandra, R. Car, C. Cavazzoni, D. Ceresoli, G. Chiarotti, M. Cococcioni, I. Dabo, A. Dal Corso, S. De Gironcoli, S. Fabris, G. Fratesi, R. Gebauer, U. Gerstmann, C. Gougoussis, A. Kokalj, M. Lazzeri, L. Martin-Samos, N. Marzari, F. Mauri, R. Mazzarello, S. Paolini, A. Pasquarello, L. Paulatto, C. Sbraccia, S. Scandolo, G. Sclauzero, A. Seitsonen, A. Smogunov, P. Umari, and R. Wentzcovitch, Quantum ESPRESSO: A modular and open-source software project for quantum simulations of materials, *J. Phys.: Condens. Matter.* **21**, 395502 (2009).

[100] P. Giannozzi, O. Andreussi, T. Brumme, O. Bunau, M. Buongiorno Nardelli, M. Calandra, R. Car, C. Cavazzoni, D. Ceresoli, M. Cococcioni, N. Colonna, I. Carnimeo, A. Dal Corso, S. de Gironcoli, P. Delugas, R. A. DiStasio Jr., A. Ferretti, A. Floris, G. Fratesi, G. Fugallo, R. Gebauer, U. Gerstmann, F. Giustino, T. Gorni, J. Jia, M. Kawamura, H.-Y. Ko, A. Kokalj, E. Küçükbenli, M. Lazzeri, M. Marsili, N. Marzari, F. Mauri, N. L. Nguyen, H.-V. Nguyen, A. Otero-della Rosa, L. Paulatto, S. Ponce, D. Rocca, R. Sabatini, B. Santra, M. Schlipf, A. Seitsonen, A. Smogunov, I. Timrov, T. Thonhauser, P. Umari, N. Vast, and S. Baroni, Advanced capabilities for materials modelling with Quantum ESPRESSO, *J. Phys.: Condens. Matter.* **29**, 465901 (2017).

[101] P. Giannozzi, O. Baseggio, P. Bonfà, D. Brunato, R. Car, I. Carnimeo, C. Cavazzoni, S. de Gironcoli, P. Delugas, F. Ferrari Ruffino, A. Ferretti, N. Marzari, I. Timrov, A. Urru, and S. Baroni, Quantum ESPRESSO toward the exascale, *J. Chem. Phys.* **152**, 154105 (2020).

[102] J. Perdew, A. Ruzsinszky, G. Csonka, O. Vydrov, G. Scuseria, L. Constantin, X. Zhou, and K. Burke, Restoring the Density-Gradient Expansion for Exchange in Solids and Surfaces, *Phys. Rev. Lett.* **100**, 136406 (2008).

[103] K. Garrity, J. Bennett, K. Rabe, and D. Vanderbilt, *Comput. Mater. Sci.* **81**, 446 (2014).

[104] R. Fletcher, *Practical Methods of Optimization*, 2nd ed. (Wiley, Chichester, 1987).

[105] I. Timrov, N. Marzari, and M. Cococcioni, HP – A code for the calculation of Hubbard parameters using density-functional perturbation theory, *Comput. Phys. Commun.* **279**, 108455 (2022).

[106] I. Timrov, F. Aquilante, L. Binci, M. Cococcioni, and N. Marzari, Pulay forces in density-functional theory with extended Hubbard functionals: from nonorthogonalized to orthogonalized manifolds, *Phys. Rev. B* **102**, 235159 (2020).

[107] M. J. Carey, F. E. Spada, A. E. Berkowitz, W. Cao, and G. Thomas, Preparation and structural characterization of sputtered coo, nio, and ni0.5co0.5o thin epitaxial films, *Journal of Materials Research* **6**, 2680 (1991).

[108] D. K. Smith and W. Newkirk, The crystal structure of baddeleyite (monoclinic ZrO_2) and its relation to the polymorphism of ZrO_2 , *Acta Crystallographica* **18**, 983 (1965).

[109] G. H. Kwei, A. C. Lawson, S. J. L. Billinge, and S. W. Cheong, Structures of the ferroelectric phases of barium titanate, *J. Phys. Chem.* **97**, 2368 (1993).

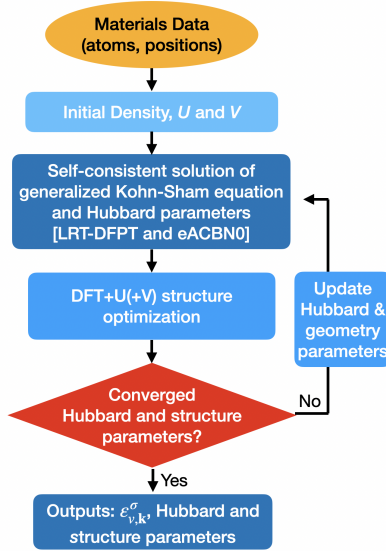


FIG. S1. Protocol for computing Hubbard parameters within the “structurally self-consistent” scheme using either LRT (DFPT) [57] or eACBN0 [44]. Total energy, U , V , and the structural parameters are iteratively updated until each meets the chosen convergence threshold.

SUPPLEMENTARY INFORMATION

Self-consistent protocol with structural relaxation

The computational workflow for the “structurally self-consistent” scheme, i.e. combining Hubbard-parameter calculations (via LRT or eACBN0) with structural relaxations, is illustrated in Fig. S1. The procedure begins with an initial crystal structure and an initial guess for the Hubbard parameters, which may be set to zero. A self-consistent DFT+ U (+ V) calculation is then performed to obtain the electronic ground state. In the case of eACBN0, the Hubbard parameters U and V are additionally computed as described in the main text. For clarity, we emphasize that LRT and eACBN0 are executed as two independent workflows.

Next, the crystal structure is optimized using DFT+ U (+ V), including Hubbard contributions to forces and stresses [66, 106], and employing the U and V values determined in the preceding step. If the updated Hubbard parameters or the relaxed geometry deviate from their previous values by more than user-defined thresholds, the cycle is repeated. This iterative loop continues until both the Hubbard parameters and the crystal structure are converged. The resulting self-consistent U and V values are then used in production calculations.

This protocol drives the system toward an energy extremum where the electronic and structural degrees of freedom are mutually consistent. Moreover, the same workflow can be applied to DFT+ U alone by simply setting $V = 0$. The LRT (DFPT) workflow is fully automated in AiiDA-Hubbard, which greatly streamlines the entire procedure [75].

Self-consistent Hubbard parameters including structural relaxation

MnO, FeO, CoO, and NiO.

For the four transition-metal oxides (TMOs) considered here, the relaxed geometries obtained with self-consistent Hubbard parameters show very good agreement with available experimental data, as illustrated in Figs. S2 and S3. These structural results are only weakly affected by the inclusion of the on-site Hubbard correction for oxygen (U_O), as evidenced by the close similarity between Fig. S2(a) and Fig. S3(a).

The Hubbard parameters, band gaps, and magnetic moments obtained from the “structurally self-consistent” scheme (see Fig. S1) follow the same qualitative trends reported in the main text for calculations performed without structural relaxations (Figs. 2 and 3). Therefore, we

conclude that full structural relaxations combined with self-consistent U and V values reliably reproduce the experimental geometries of MnO, CoO, and NiO, and that the associated electronic properties remain largely unchanged upon including structural relaxations.

ZrO₂ and BaTiO₃.

Figure S4 summarizes the results for the nominally d^0 system ZrO₂ obtained using the “structurally self-consistent” scheme (see Fig. S1). The fully relaxed structural parameters show good agreement with experimental data, as illustrated in Figs. S4(a) and (d). Consistently with results from the “self-consistent” scheme (no DFT+ U + V structural relaxation) presented in Figs. 4 and 5 of the main text, the LRT approach yields a finite U_{Zr} value due to the response of small but non-zero d occupations, whereas ACBN0 gives a vanishing value. The largest contribution to the band-gap correction arises from U_O and $V_{Zr,O}$ (particularly within the ACBN0 scheme) which brings the calculated band gap closer to the experimental value. In contrast, the lattice constant is influenced mainly by the U_{Zr} correction, with only minor sensitivity to U_O and $V_{Zr,O}$.

Next, we consider BaTiO₃, which, like ZrO₂, has a nominal d^0 configuration. The results, shown in Fig. S5, follow trends consistent with those discussed in the main text. For the structural properties, when the on-site oxygen Hubbard correction (U_O) is excluded, LRT-based DFT+ U + V and eACBN0-based DFT+ U and DFT+ U + V all predict a rhombohedral distortion with an angle below 90° (see Fig. S5(b)). When U_O is included, only the eACBN0-based DFT+ U + V scheme retains this rhombohedral distortion (see Fig. S5(f)).

ZnO.

Figure S6 presents the results for ZnO, a system with a nominally filled d^{10} shell, obtained using the “structurally self-consistent” scheme (see Fig. S1). In line with the findings reported in the main text (without DFT+ U + V structural relaxations), the LRT approach again yields an unphysically large value of U_{Zn} . Nevertheless, this large U_{Zn} has only a minor effect on both the lattice constants and the band gap, because the Zn-3d states are fully occupied and play essentially no role in the chemical bonding or the states around the band edges.

As shown in Figs. S6(d)–(f), and consistent with Fig. 9 in the main text, including U_O increases the band gap significantly. However, while LRT leads to a band gap that substantially overestimates the experimental value, the ACBN0 scheme yields a band gap in very good agreement with experiment.

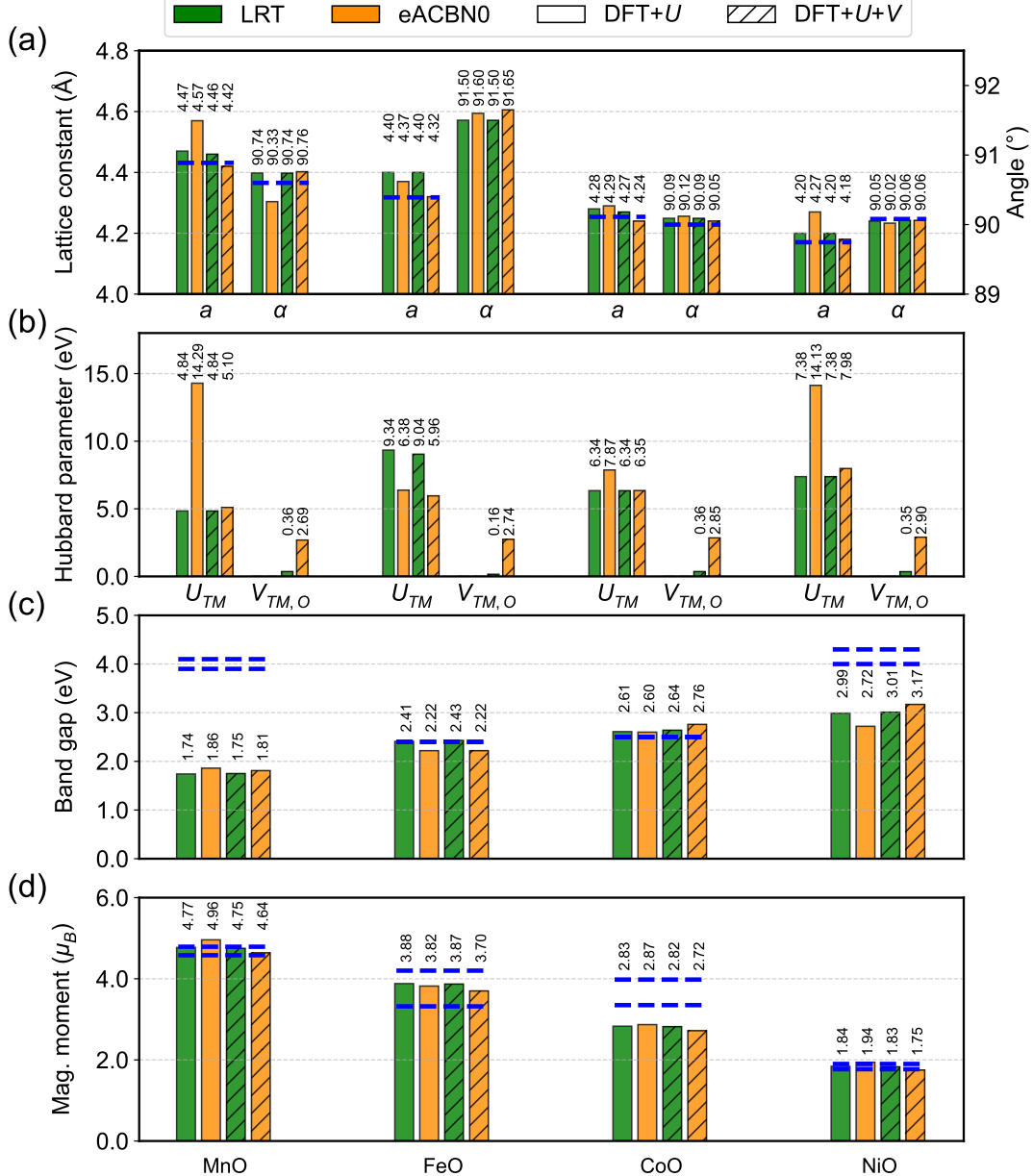


FIG. S2. DFT+ U and DFT+ $U+V$ “structurally self-consistent” calculations for TMOs without the oxygen Hubbard correction (U_O). (a) Lattice constant a and rhombohedral angle α , (b) on-site Hubbard parameter U_{TM} for the TM-3d states and inter-site parameter $V_{TM,O}$ between TM-3d and O-2p states, (c) band gap, and (d) magnetic moment. LRT and eACBN0 indicate the method used to obtain the Hubbard parameters. Experimental lattice constants and rhombohedral angles for MnO [81], FeO [85], CoO [107], and NiO [81] are shown as dashed blue lines in panel (a); for FeO, the values correspond to $\text{Fe}_{0.943}\text{O}$. Experimental band gaps and magnetic moments for MnO [79–82], FeO [83–85], CoO [86–88], and NiO [79, 81, 82, 89] are indicated by dashed blue lines in panels (c) and (d), respectively.

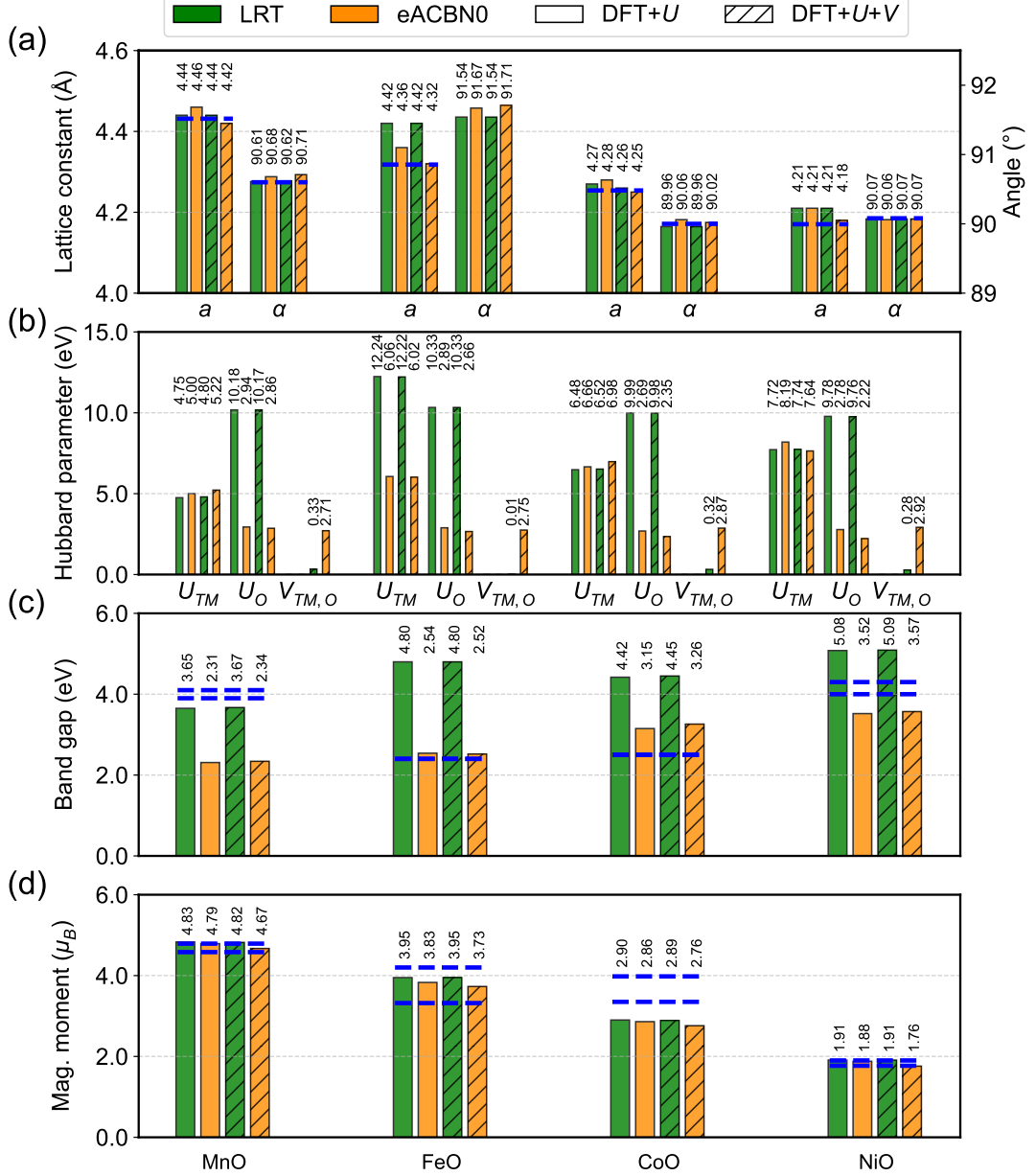


FIG. S3. DFT+ U and DFT+ $U+V$ “structurally self-consistent” calculations for TMOs with the oxygen Hubbard correction (U_O). The remainder of the caption is analogous to Fig. S2.

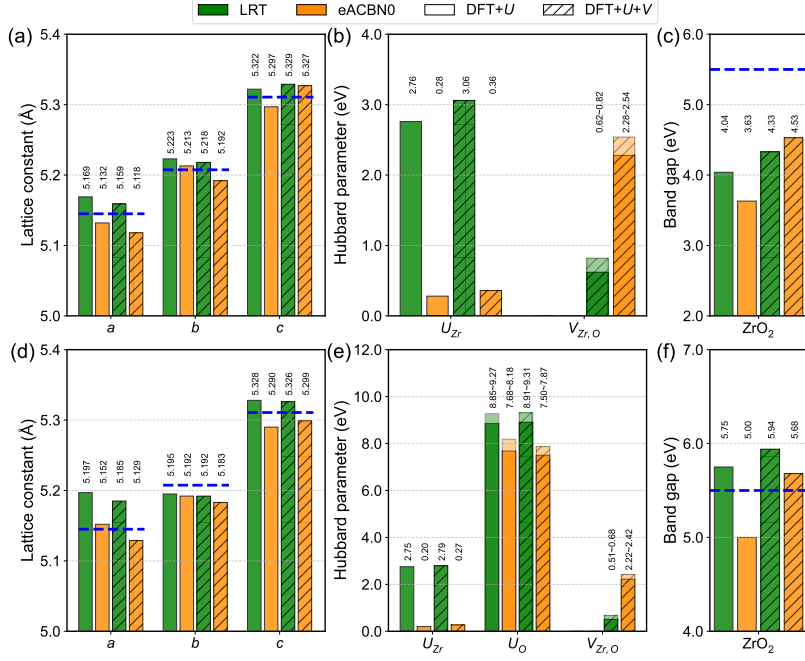


FIG. S4. DFT+U and DFT+U+V “structurally self-consistent” calculations for ZrO₂ without U_O [panels (a)–(c)] and with U_O [panels (d)–(f)]. Panels (a) and (d) show the lattice constants a , b , and c , with experimental values [108] indicated by dashed blue lines. Panels (b) and (e) display the on-site Hubbard parameters U_{Zr} and U_O for Zr-4d and O-2p states, respectively, as well as the inter-site parameter $V_{Zr,O}$ between Zr-4d and O-2p states. Panels (c) and (f) show the corresponding band gaps, with the experimental band gap [91] marked by a dashed blue line.

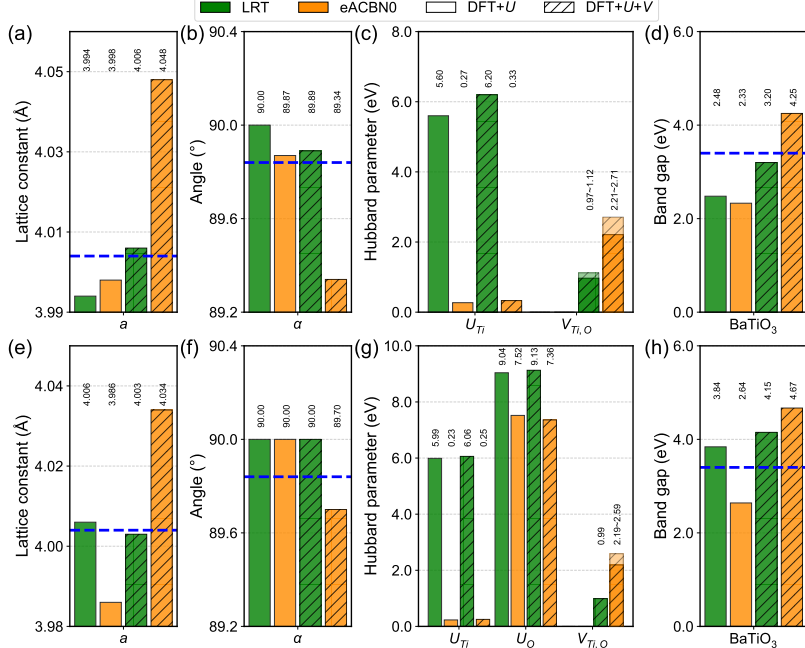


FIG. S5. DFT+U and DFT+U+V “structurally self-consistent” calculations for BaTiO₃ without U_O [panels (a)–(d)] and with U_O [panels (e)–(h)]. Panels (a) and (e) show the lattice constant a , while panels (b) and (f) display the rhombohedral angle α , with experimental values [109] indicated by dashed blue lines. Panels (c) and (g) present the on-site Hubbard parameters U_{Ti} and U_O for Ti-3d and O-2p states, respectively, as well as the inter-site parameter $V_{Ti,O}$ between Ti-3d and O-2p states. Panels (d) and (h) show the corresponding band gaps, with the experimental band gap [94] marked by a dashed blue line.

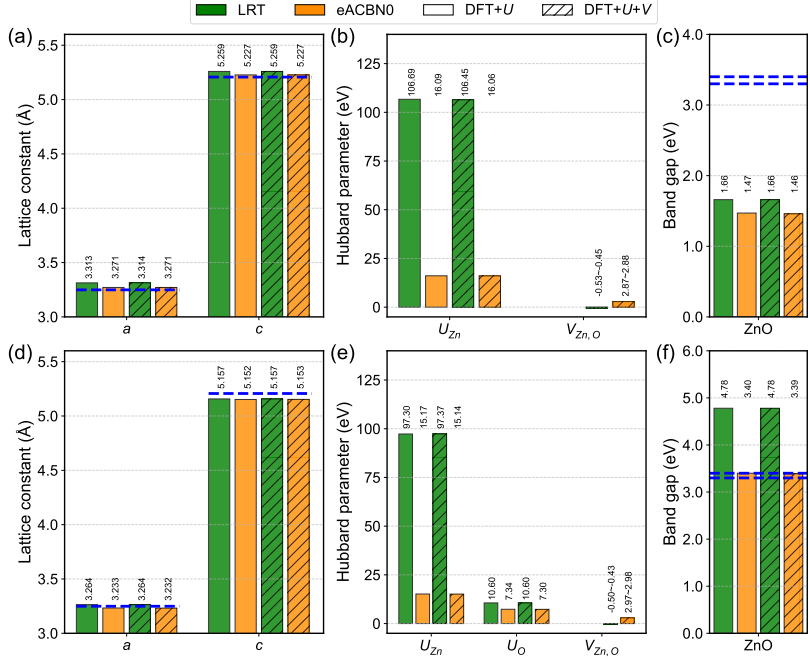


FIG. S6. DFT+ U and DFT+ U + V “structurally self-consistent” calculations for ZnO without U_O [panels (a)–(c)] and with U_O [panels (d)–(f)]. Panels (a) and (d) show the lattice constants a and c . Panels (b) and (e) display the on-site Hubbard parameters U_{Zn} and U_O for Zn-3d and O-2p states, respectively, along with the inter-site parameter $V_{Zn,O}$ between Zn-3d and O-2p states. Experimental lattice constants and band gaps [95–98] are indicated by dashed lines in panels (a) and (d), and panels (c) and (f), respectively.